Journal of Physics D:
Applied Physics

TOPICAL REVIEW • **OPEN ACCESS**

Recent progress on multiferroic hexagonal rare-earth ferrites (h-RFeO$_3$, R = Y, Dy-Lu)

To cite this article: Xin Li *et al* 2025 *J. Phys. D: Appl. Phys.* **58** 073003

OPEN ACCESS
IOP Publishing
Journal of Physics D: Applied Physics
J. Phys. D: Appl. Phys. **58** (2025) 073003 (20pp)
https://doi.org/10.1088/1361-6463/ad97c5

Topical Review

Recent progress on multiferroic hexagonal rare-earth ferrites (h-RFeO$_3$, R = Y, Dy-Lu)

Xin Li[1], **Yu Yun**[1,2,*] **and Xiaoshan Xu**[1,3,*]

[1] Department of Physics and Astronomy, University of Nebraska, Lincoln, NE 68588, United States of America
[2] Department of Mechanical Engineering & Mechanics, Drexel University, Philadelphia, PA 19104-2875, United States of America
[3] Nebraska Center for Materials and Nanoscience, University of Nebraska, Lincoln, NE 68588, United States of America

E-mail: yy549@drexel.edu and xiaoshan.xu@unl.edu

Received 17 July 2024, revised 8 October 2024
Accepted for publication 27 November 2024
Published 9 December 2024

Abstract

Multiferroic hexagonal rare-earth ferrites (h-RFeO$_3$, R = Sc, Y, and rare earth), in which the improper ferroelectricity and canted antiferromagnetism coexist, have been advocated as promising candidates to pursue the room-temperature multiferroics, because of strong spin-spin interaction. The strong interactions between the ferroic orders and the structural distortions are appealing for high-density, energy-efficient electronic devices. Over the past decade, remarkable advances in atomic-scale synthesis, characterization, and material modeling enable the significant progresses in the understanding and manipulation of ferroic orders and their couplings in h-RFeO$_3$ thin films. These results reveal a physical picture of rich ferroelectric and magnetic phenomena interconnected by a set of structural distortions and spin-lattice couplings, which provides guidance for the control of ferroic orders down to the nano scale and the discovery of novel physical phenomena. This review focus on state-of-the-art studies in complex phenomena related to the ferroelectricity and magnetism as well as the magnetoelectric couplings in multiferroic h-RFeO$_3$, based on mostly the recent experimental efforts, aiming to stimulate fresh ideas in this field.

Keywords: multiferroic, hexagonal, ferrites, thin film, magnetoelectric, complex oxide, ferroelectric

* Authors to whom any correspondence should be addressed.

1. Introduction and basics

With the developments of Big Data and Internet of Things, there has been a widespread and growing demand for a device paradigm shift toward high-integration, energy-efficient, and multifunctional devices. Among the pepped up advanced materials, multiferroic materials, based on spins, electric dipoles, and elastic distortions, have attracted tremendous attention due to their exotic physical properties and novel functionalities on the macroscopic and microscopic level, holding great promise for future low-power electronic products [1–5]. The coexistence of magnetism and ferroelectricity in a single-phase material, however, is rare in nature, especially above room temperature [6–10]. Over the past decades, significant efforts have been devoted on multiferroic complex oxides to understand the origin of the ferroic orders and their couplings toward realizing strong magnetoelectric couplings at high temperatures [11–13]. A plethora of phenomena have been discovered on different levels, such as polar vortex [14–16], domain-wall conductivity [17–20], magnetoelectric coupling [21], which have expanded the conventional understanding of ferroic orders and driven the exploration of novel physical phenomena and functionalities which may be harnessed for practical multifunctional device applications [22–24].

Generally, single-phase multiferroic compounds can be classified as two types, type-I and type-II multiferroics, depending on whether the ferroelectric and magnetic states appear independently [25]. In particular, type-II multiferroics refer in particular to magnetism-driven multiferroics, wherein the magnetic order leads to an inversion symmetry breaking and thus generates the ferroelectricity. All other multiferroics can be categorized as type-I multiferroics, in which the ferroelectricity usually is stabilized at higher temperature, while the appearance of magnetic order is observed at lower temperature. Hexagonal rare-earth ferrites (h-$R$$FeO_3$, R = Sc, Y, and rare earth), which are categorized as type-I multiferroics, have the isomorphic crystal structure with that of h-$R$$MnO_3$ [26–28]. In comparison with their manganites counterparts, h-$R$$FeO_3$ have stronger magnetic order due to the enhanced exchange interaction between Fe sites and exhibit finite spontaneous magnetizations [29–31]. Among the most intriguing is that both spontaneous polarization and magnetization originate from the same non-polar structural distortion. Consequently, the structural distortion has been explored as a medium to couple magnetism and ferroelectricity [32], promising a highly designable and tunable multiferroicity. For instance, multiple means have been used to tune the structural distortion in epitaxial thin films, such as interface, strain, and doping [33–38].

The hexagonal rare-earth ferrites exhibit distinct crystal structure and symmetry from their perovskite counterparts. The hexagonal crystal structure (space group $P6_3cm$) serves as the foundation for the polar and spin orders in multiferroic h-$R$$FeO_3$. The unit cell of h-$R$$FeO_3$ is composed of the triangular lattice of FeO_5 bipyramids, which is sandwiched by the rare earth layers, as shown in figure 1(a). For two consecutive FeO_5 layers, the two triangle lattices rotate 60° with respect to each other. The lattice distortion relative to the high-temperature paraelectric phase structure (space group $P6_3/mmc$) can be decomposed into three modes [39, 40]. The K_3 mode corresponds to rotation of FeO_5 bipyramids, which can be quantified by the magnitude (Q) and rotation angle (ϕ_Q) of apical oxygen (see figure 1(a)), associated with the corrugation of rare earth layer (see figure 1(b)); Γ_2^- mode corresponds to the displacement of atoms along the c axis that generates a dipole moment; K_1 mode corresponds to the in-plane displacement of Fe in the FeO_5 bipyramids, reducing their point-group symmetry from D_{3h} to C_S [29–31].

The non-polar K_3 mode induces the polar Γ_2^- mode which leads to a buckling of oxygen polyhedral (FeO_5 bipyramid) and trimerization of apical oxygen anions, consequently giving rise to an offset of rare-earth cations and resulting spontaneous polarization. Thus, the spontaneous polarization is proportional to the magnitude of the Γ_2^- mode below Curie temperature (T_c) of ∼1000 K [39, 41]. So, the ferroelectricity of h-$R$$FeO_3$ is called 'improper' or geometric ferroelectricity [42]. On the other hand, for magnetism, the K_3 mode breaks the three-fold rotational symmetry of the interlayer exchange interaction and determines the three-dimensional magnetic ordering temperature [29–31]. The in-plane spins along the (100) direction is energetically more favorable than the out-of-plane spins owing to their interlayer exchange interaction and K_1 distortion [43]. Rotation of the FeO_5 bipyramids leads to the canting of the Fe spins toward the out-of-plane direction due to the spin-orbit coupling and Dzyaloshinskii–Moriya (DM) interactions [32], corresponding to a weak ferromagnetism or canted antiferromagnetism. Therefore, the K_3 distortion, as a lattice degree of freedom, bridges the ferroelectricity and magnetism in h-$R$$FeO_3$.

Despite great promises and fascinating features, unlike their manganites cousins, the ground state of $R$$FeO_3$ ferrites in bulk are commonly orthorhombic phase rather than hexagonal phase, which is metastable state [44]. This hinders the understanding of physical mechanism and the discovery and control of new functionalities in h-$R$$FeO_3$. Strain engineering or mechanical boundary conditions, which is imposed by the semi-infinite substrate, such as YSZ (111) and Al_2O_3 (0001) substrates [29, 45], is leveraged to stabilize the metastable hexagonal phase of $RFeO_3$, providing a pathway to study the fundamental physics mainly about magnetism and crystal structure. More recently, advances in atomic-scale thin film growth, structural design, and characterization technique enable a electrical measurements with an oxide bottom electrode and facilitate a large degree of control over ferroelectric function, offering new opportunities to further understanding and engineering their ferroelectric, magnetic, and multiferroic properties in concert with multiscale modeling. Although significant efforts are being devoted, a comprehensive overview is still missing on recent developments and breakthroughs in hexagonal rare-earth ferrites.

In this review, we focus on the advancement of understanding on the physical mechanisms of multiferroicity from the viewpoint of experimentalist, in contrast to previous reviews

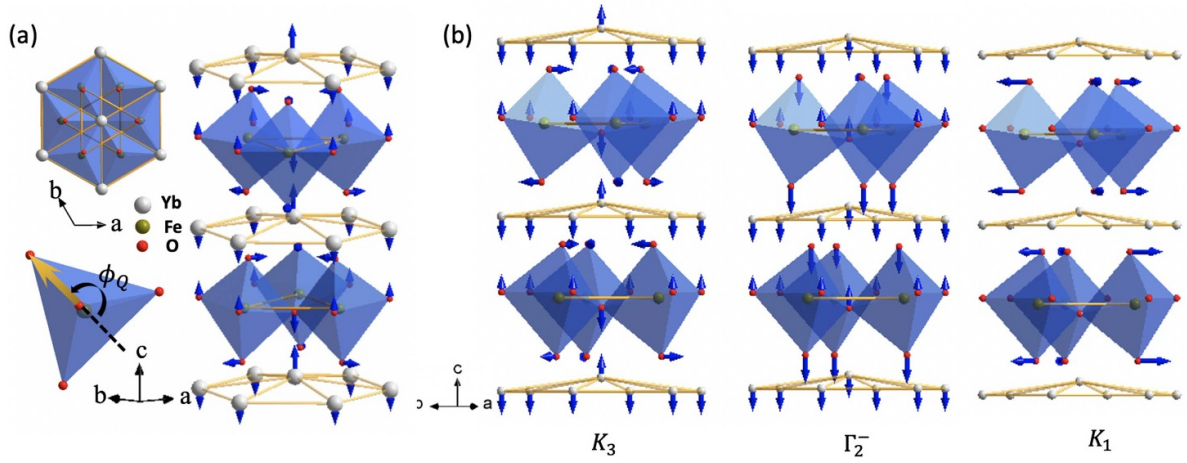

Figure 1. (a) Schematic of atomic structure of h-$RFeO_3$. (b) The structure distortions for K_3, Γ_2^- and K_1 mode, respectively.

which focus more on stabilization of the hexagonal structure of RFeO$_3$ and characterization of basic ferroic properties [44, 46, 47]. More explicitly, we will discuss experimental advances that lead to more insights on the underpinning mechanisms of improper ferroelectricity in ultrathin films, ferroelectric switching dynamics, as well as on the importance of spin-lattice coupling for almost all aspects of magnetism, including magnetic ordering temperature, single-ion magnetic anisotropy, and weak-ferromagnetism.

2. Improper ferroelectricity

The improper ferroelectricity of h-RFeO$_3$ is expected to be similar to that in h-RMnO$_3$, which has been established decades ago [28, 48]. The implication of improper ferroelectricity, including its effect on depolarization field and the consequential absence of critical thickness, as well as its behavior under strain and at interfaces, are intriguing. The recent advances in atomic-scale modulation of h-RFeO$_3$ in epitaxial thin films, as well as the combination of phenomenological models and experiments, push forward the understanding on these implications, highlighting the application potentials of h-RFeO$_3$ as improper ferroelectrics toward device miniaturization and high energy efficiency.

2.1. Landau theory for improper ferroelectricity in h-RFeO$_3$

The order parameter of the improper ferroelectricity of h-RFeO$_3$ is the nonpolar K_3 distortion, in which the collective rotation of the FeO$_5$ bipyramids contributes to the geometric field to the nearby rare earth layer [48], leading to the spontaneous polarization (polar Γ_2^- mode). Figure 2(a) shows the part of K_3 distortion in terms of the displacement of apical oxygen in FeO$_5$; the direction of the displacement is defined by the angle ϕ_Q. The free energy from Landau theory has been constructed as [50]:

$$G = \frac{a}{2}Q^2 + \frac{b}{4}Q^4 - gQ^3P\cos(3\phi_Q) + \frac{g'}{2}Q^2P^2 + \frac{a_p}{2}P^2 - EP \quad (1)$$

where Q is magnitude of the K_3 distortion, P is the polarization, a, b, g, g', a_p are coefficients. The first and second terms correspond to K_3 mode only, the third and fourth terms describe the coupling between the K_3 and the Γ_2^- mode, the fifth term is for the Γ_2^- mode, and the last term corresponds to electrostatic energy. Without electric field, the energy landscape has six-fold symmetry with energy minimum at $\phi_Q = n\frac{\pi}{3}$ (n is integer), as shown in figure 2(b). The polarization can be found as:

$$P = \frac{gQ^3\cos(3\phi_Q)}{g'Q^2 + a_P}. \quad (2)$$

With electric field, the symmetry of the energy landscape reduces to a three-fold rotational symmetry (see figure 2(c)) [51]. Moreover, compared to the polarization-dependent double-well free energy landscape in proper ferroelectrics, the free energy of h-RFeO$_3$ depends on polarization, Q, and ϕ_Q (see figure 2(d)), since the primary order parameter is the structural distortion rather than electrical polarization. Nevertheless, the transition from the ferroelectric phase to the paraelectric phase still corresponds to the vanishing order parameter [39]. In other words, the Landau coefficient in first term can be approximately written as $a(T_c - T)$. Above T_c, the energy minimum is at $Q = 0$, corresponding to the paraelectric phase with space group $P6_3/mmc$. Figure 2(f) shows the temperature-dependent Q and P from the Landau theory [49].

2.2. Impacts of depolarization field on improper ferroelectricity in h-RFeO$_3$ films

The improper ferroelectricity in h-RFeO$_3$ implies the insensitivity of order parameter (K_3 distortion) to the depolarization field and the potential absence of critical thickness [53, 54], since its primary order parameter is structural distortion, in contrast to proper ferroelectrics [55–57]. Experimentally, the depolarization field can be manipulated by inserting the dielectric (DE) layer between bottom electrode and ferroelectric (FE) layer. As shown in figure 3(a), the epitaxial film of h-YbFeO$_3$ was grown on $CoFe_2O_4$

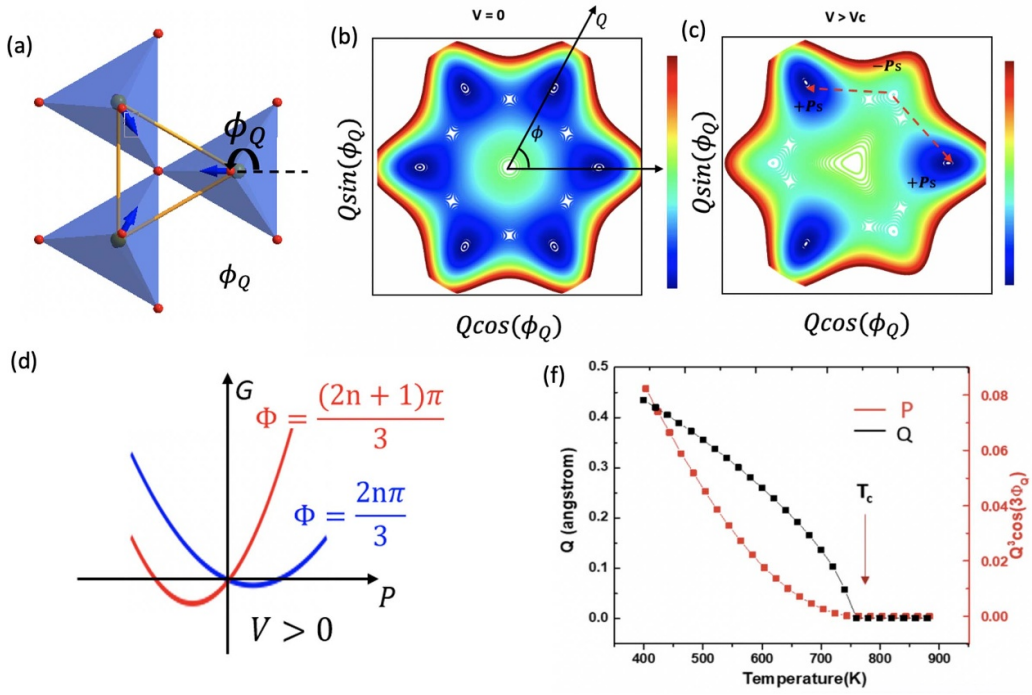

Figure 2. (a) The definition of order parameters of K_3 distortion. (b) The energy landscape of *h*-*R*FeO_3 without and (c) with electric field. (d) Schematic polarization-dependent free energy with constant phase angle. (e) The temperature-dependent paraelectric-ferroelectric phase transition for h-*Sc*FeO_3. (f) Reprinted from [49], with the permission of AIP Publishing.

(111)/ $La_{2/3}Sr_{1/3}MnO_3$(LSMO)/$SrTiO_3$(STO)(111), in which the $CoFe_2O_4$ layer serves as both the dielectric layer to tune depolarization field and the buffer layer to mitigate the lattice mismatch with LSMO [57]. Figure 2(b) shows the schematic of the potential distribution in a FE/DE bilayer system under the short-circuit condition. The ferroelectric hysteresis at cryogenic temperature (20 K), as shown in figure 3(c), indicates that the lower FE/DE thickness ratio (t_F/t_D) would suppress the remnant polarization (P_r) and enhance the coercive field, which is qualitatively similar to the trend in proper ferroelectrics. Moreover, the suppression of P_r with decreasing t_F/t_D does not follows the model for single-domain case directly, and the deviation of experimental results from theoretical fits suggests that the h-$YbFeO_3$ films enter the multidomain states when t_F/t_D is between 1 and 5 (see figure 3(d)). This manifests that domain structures of improper ferroelectrics are also influenced by electrical boundary conditions. In addition, when the $CoFe_2O_4$ is fixed at ∼10 nm, the polarization for the thinnest h-$YbFeO_3$ (≈3 u.c.) films in figure 3(d) is still finite, suggesting absence of critical thickness.

2.3. *Interfacial clamping in ultrathin h-*R*FeO_3 films*

Although h-*R*FeO_3 is believed to have no critical thickness [53], the interfacial clamping effect causes a 'practical' critical thickness below which the order parameter Q of the K_3 distortion vanishes [52, 54]. Figure 4(a) shows the schematic phase diagram for the phase transition with temperature and thickness as two independent variables. Figures 4(b) and (c) demonstrate the cross-section HADDF-STEM images for h-$LuFeO_3$/YSZ [58] and h-$YbFeO_3$/CFO interfaces [52], in which the corrugation of initial rare earth layer is greatly suppressed; the thickness dependent Q' (the displacement of the R atoms which is proportional to Q) calculated from the image of figure 4(c) is presented in figure 4(d). Thus, beyond electrical boundary condition, mechanical boundary condition also has a remarkable impact on the structure and electrical property of improper ferroelectrics. The suppression of Q' near the interface by interfacial clamping could induce additional elastic energy, which can be expressed as [49]:

$$f_{\text{elastic}} = k\left(\frac{\partial Q}{\partial z}\right)^2 \tag{3}$$

in which k is the stiffness coefficient, z is along c-axis of h-$RFeO_3$. Combining with free energy in equation (1), the thickness-dependent Q follows the equation:

$$Q(z,T) = Q_\infty(T)\frac{1-\exp\left(-\frac{z}{\zeta(T)}\right)}{1+\exp\left(-\frac{z}{\zeta(T)}\right)},$$
$$with\begin{cases} Q_\infty(T) = \sqrt{\frac{-a_0}{b}}\sqrt{1-\frac{T}{T_s}} = Q_0\sqrt{1-\frac{T}{T_s}} \\ \zeta(T) = \sqrt{\frac{k}{-a_0}}\sqrt{\frac{T_s}{T_s-T}} = \zeta_0\sqrt{\frac{T_s}{T_s-T}} \end{cases} \tag{4}$$

in which z is the film thickness, T is the temperature. $a_0 < 0$ and $b > 0$ are coefficients of Landau theory, k is the stiffness coefficient at the interface, T_s is the Curie temperature of bulk state, and ζ_0 is the characteristic length of interfacial clamping

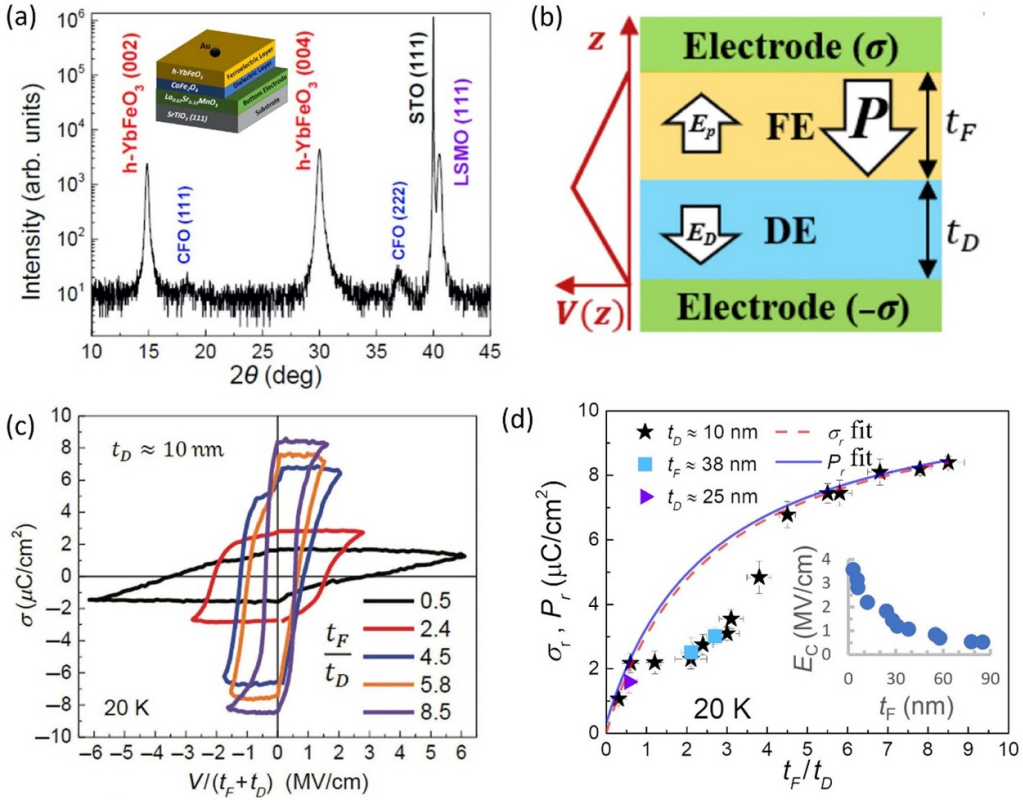

Figure 3. (a) x-ray θ-2θ scan for h-$YbFeO_3$/ $CoFe_2O_4$/LSMO/STO (111) film. (b) Schematic diagram for the ferroelectric/dielectric system and related potential distribution. (c) Ferroelectric hysteresis loops of h-$YbFeO_3$ with various ratios between the thickness of ferroelectric and dielectric layers at 20 K. (d) The thickness-dependent remanent polarization and related fit for h-$YbFeO_3$ films, the inset is thickness-dependent coercive field. (a)–(d) Reprinted figure with permission from [52], Copyright 2022 by the American Physical Society.

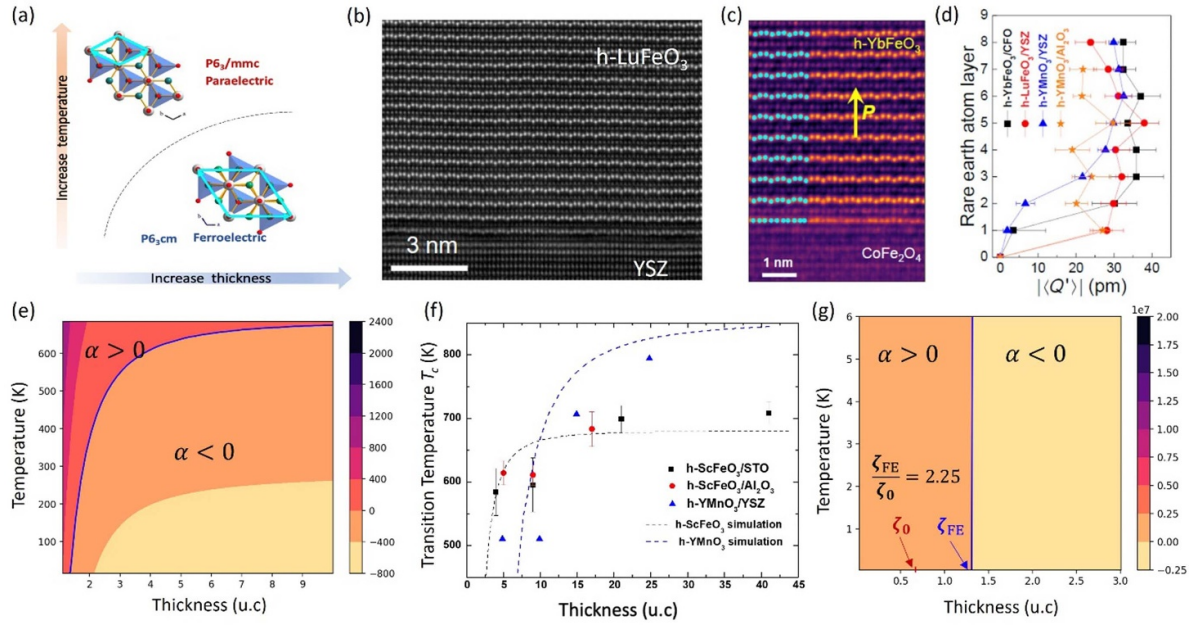

Figure 4. (a) Schematic for the temperature and thickness-dependent paraelectric-ferroelectric phase transition in h-$RFeO_3$ film. (b) h-$LuFeO_3$/YSZ and (c) h-$YbFeO_3$/$CoFe_2O_4$ interfaces. (d) The thickness-dependent Q. (e) Theoretical phase diagram for paraelectric-ferroelectric phase transition. (f) Thickness-dependent Tc in h-$ScFeO_3$ thin film. (g) The correlation between ferroelectric critical thickness (ζ_{FE}) and effective thickness of interfacial clamping layer (ζ_0). (a) and (e)–(g) Reprinted from [49], with the permission of AIP Publishing. (b) Reprinted figure with permission from [58], Copyright 2017 by the American Physical Society. (c) and (d) Reprinted figure with permission from [52], Copyright 2022 by the American Physical Society.

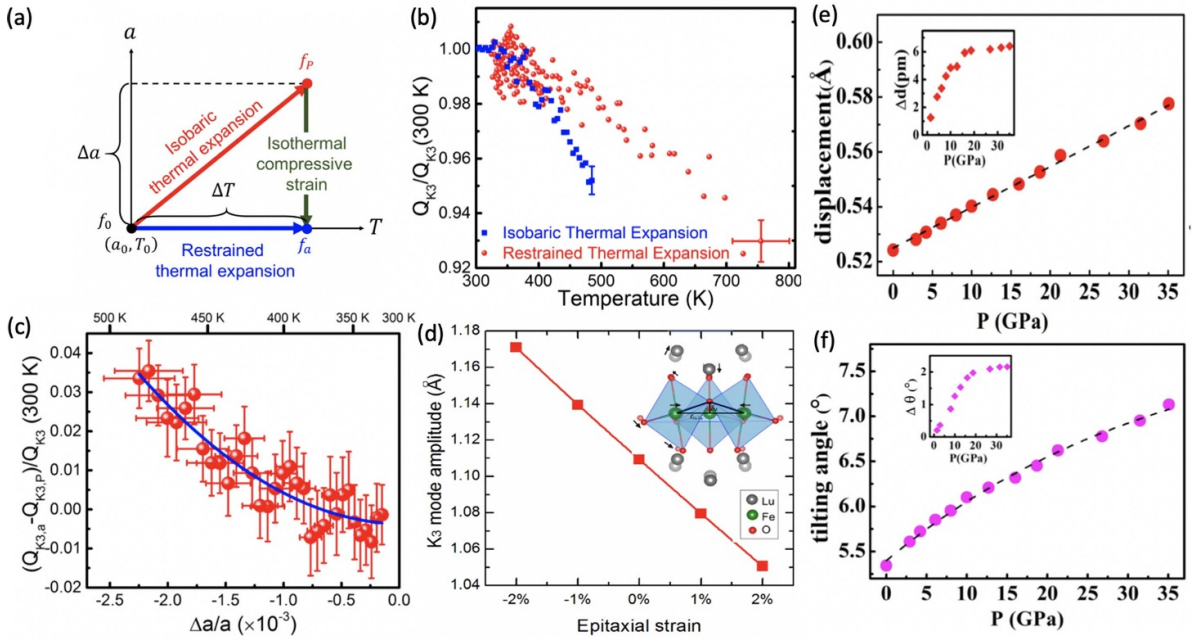

Figure 5. (a) Schematic of isobaric and restrained thermal expansion in (a, T) space. (b) The temperature dependent K_3 distortion for isobaric and restrained thermal expansion. (c) The effect of isothermal compressive strain on K_3 distortion. (d) The effect of biaxial compressive strain on K_3 distortion by calculation. (e) The pressure dependent displacement of rare earth and (f) tilt angle of FeO_5. (a)–(d) Reprinted figure with permission from [59], Copyright 2017 by the American Physical Society. (e) and (f) Reprinted figure with permission from [60], Copyright 2019 by the American Physical Society.

at $T = 0$ K. The thickness and temperature-dependent phase transition can be further described as:

$$\alpha\left(t_F, T\right) = T - T_S\left[1 - 2\zeta_0^2\,\frac{C_2\left(t_F, T\right)}{C_1\left(t_F, T\right)}\right] = 0 \tag{5}$$

with

$$\begin{cases} C_1\left(t_F, T\right) = \int_0^{t_F}\left(\frac{1-\exp\left(-\frac{z}{\zeta(T)}\right)}{1+\exp\left(-\frac{z}{\zeta(T)}\right)}\right)^2 dz \\ C_2\left(t_F, T\right) = \int_0^{t_F}\frac{\left(\frac{2}{\zeta}*exp\left(-\frac{z}{\zeta(T)}\right)\right)^2}{\left(1+\exp\left(-\frac{z}{\zeta(T)}\right)\right)^4} dz \end{cases}. \tag{6}$$

Therefore, the boundary of phase transition, as shown in figure 4(e), is determined by T_s and ζ_0 simultaneously. The phase transition based on *in-situ* reflection high-energy electron diffraction (RHEED) was observed in h-$ScFeO_3$ films on both STO (111) and Al_2O_3 (001) substrates, which can be fitted using the above phenomenological model (see figure 5(f)). Moreover, this model also indicates that the 'practical' critical thickness of h-$R$$FeO_3$ is proportional to the characteristic thickness of interfacial clamping (see figure 5(g)). Therefore, to remove the interfacial clamping-induced critical thickness in ultrathin limit of h-$R$$FeO_3$ films, it is required for lattice-matched substrates or freestanding membranes released from substrates.

2.4. Strain effects on improper ferroelectricity

Strain engineering, as a powerful strategy, could be utilized to stabilize the crystal structure that is unstable in bulk and tune the ordering temperatures and electronic states [61]. Owing to the nature of improper ferroelectrics linked with the K_3 distortion, strain engineering serves as a more effective way to modulate improper ferroelectricity in h-$R$$FeO_3$, compared to proper ferroelectrics. Experimentally, the control of strain (gradients) can be realized by varying misfit strain imposed by various substrates [29], chemical doping [30, 62], inserting buffer layer [52], changing thicknesses [63], and hydrostatic pressure [60, 64].

The misfit strain originates from the lattice mismatch at the interface, which is also susceptible to the temperature due to thermal expansion [59]. For isobaric thermal expansion, both a and c of h-$R$$FeO_3$ increase with temperature. On the other hand, if only the film is heated (substrate remains the same temperature), the in-plan lattice constant (a) is locked by the substrate while the out-of-plane lattice constant (c) is free to changes, corresponding to restrained thermal expansion. By comparing the isobaric thermal expansion and the restrained thermal expansion, the effect of isothermal strain can be detected, as illustrated in figure 5(a). As shown in figure 5(b), with the increase of temperature, both the isobaric and restrained thermal expansion could lead to the decrease of Q for K_3 distortion, but the change of Q is larger for isobaric thermal expansion. Combining the two types of thermal expansions, we extract the isothermal strain $|\Delta a/a|$ and its effect on Q,

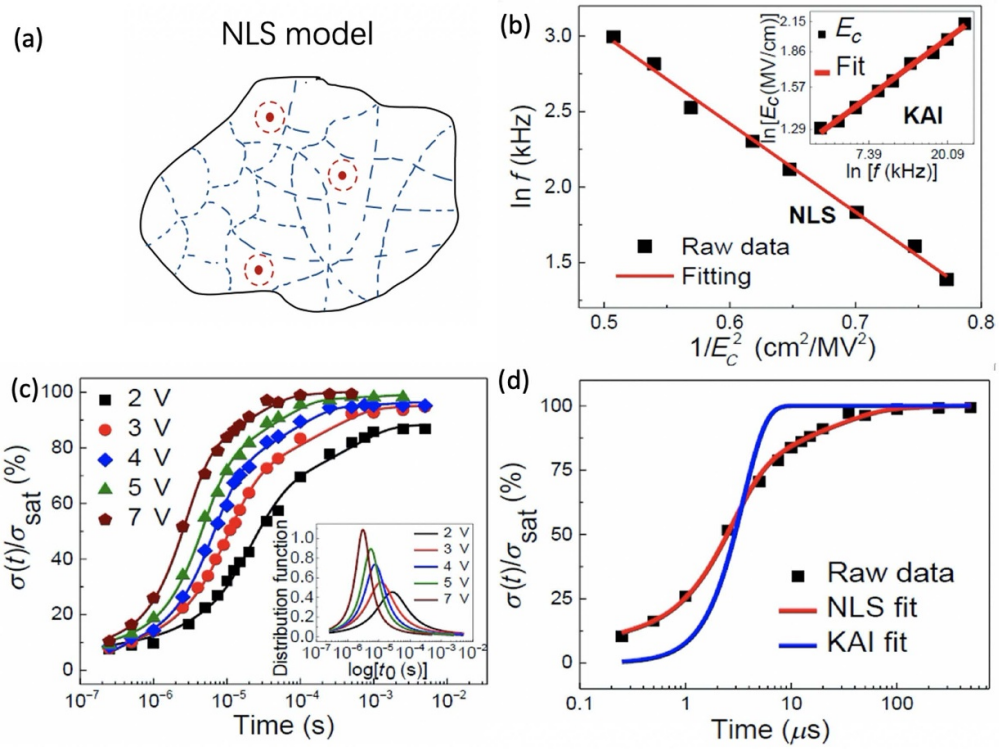

Figure 6. (a) Schematic diagram of the NLS model. (b) The frequency-dependent coercive field for h-$YbFeO_3$ film and related theoretical fitting. (c) The time-dependent polarization under different voltage for h-$YbFeO_3$ and (d) related fitting by NLS and KAI model. (b)–(d) Reprinted figure with permission from [52], Copyright 2022 by the American Physical Society.

as shown in figure 5(c). These results imply that the in-plane compressive strain enhances the K_3 distortion. The first-principles calculations corroborate the effect of epitaxial strain, as shown in figure 5(d). As illustrated in the inset of figure 5(d), under the in-plane compressive strain, the oxygen atom at the center of the trimer, which is shared by three bipyramids, moves up, while the other oxygen atoms in the bases of the three bipyramids all move down, corresponding to enhancement of the K_3 distortion. Since the polarization is proportional to Q^3 (see equation (2)), the in-plane compressive strain is expected to enhance the ferroelectricity polarization.

In addition, the isovalent chemical substitution (replacing cations with the different ionic radius but the same valence) can tune the lattice constant, corresponding to the chemical strain [30, 62]. Furthermore, the hydrostatic pressure can modulate strain by reducing both lattice constants a and c and modulate the c/a ratio. Since Fe 3d—O 2p hybridization prefers to be along the c axis, the out-of-plane lattice constant is more stable against pressure. As shown in figures 5(e) and (f), based on density function theory (DFT) calculation, as the pressure increases from 0 to 35 Ga, both the displacement in rare earth layer and the tilt angle of FeO_5 bipyramids increase, which is verified by the experimental results qualitatively (see insets of figures 5(e) and(f)) [60].

2.5. Ferroelectric switching dynamics in h-RFeO_3 films

The ferroelectric switching mechanism in the single crystal of bulk hexagonal manganites is usually described by the Kolmogorov-Avrami-Ishibashi (KAI) model [65], which is strongly correlated with the domain wall motion, wherein the six-fold ferroelectric vortex is pinned at the defect site [66–68]. By contrast, the small grains (∼10 nm) and the existence of interface in thin-film h-$R$$FeO_3$ favors the switching modes described by the nucleation limited switching (NLS) model [69]. The NSL model treats the polarization switching as inhomogeneous nucleation, as illustrated in figure 6(a), with a distribution of nucleation time. The frequency dependent-coercive field can be fitted by both the Ishibashi-Orihara model ($E_C \propto f^{\beta}$, with $\beta = 0.28$) and the Du-Chen model ($\ln f_0 + \alpha/E_C^2$) [70, 71], which are based on the KAI and the NLS models respectively. Moreover, the time-dependent change of polarization can be well fitted by the NLS model (see figures 6(c) and (d)), indicating that the nucleation process may dominate over the domain wall motion in h-$R$$FeO_3$ films, although the domain wall motion and homogeneous switching cannot be fully excluded [72].

2.6. Quantification of K_3 distortion from STEM image

Since the K_3 distortion plays a key role in determining the improper ferroelectricity of h-$R$$FeO_3$, the direct mapping of order parameters (Q, ϕ_Q) is essential to reveal the behavior of ferroelectric domains or vortex and examine the proposed model from the Landau theory [49–51]. For h-$R$$FeO_3$, the displacement of rare earth (u) can be connected to the K_3 distortion as [73, 74]:

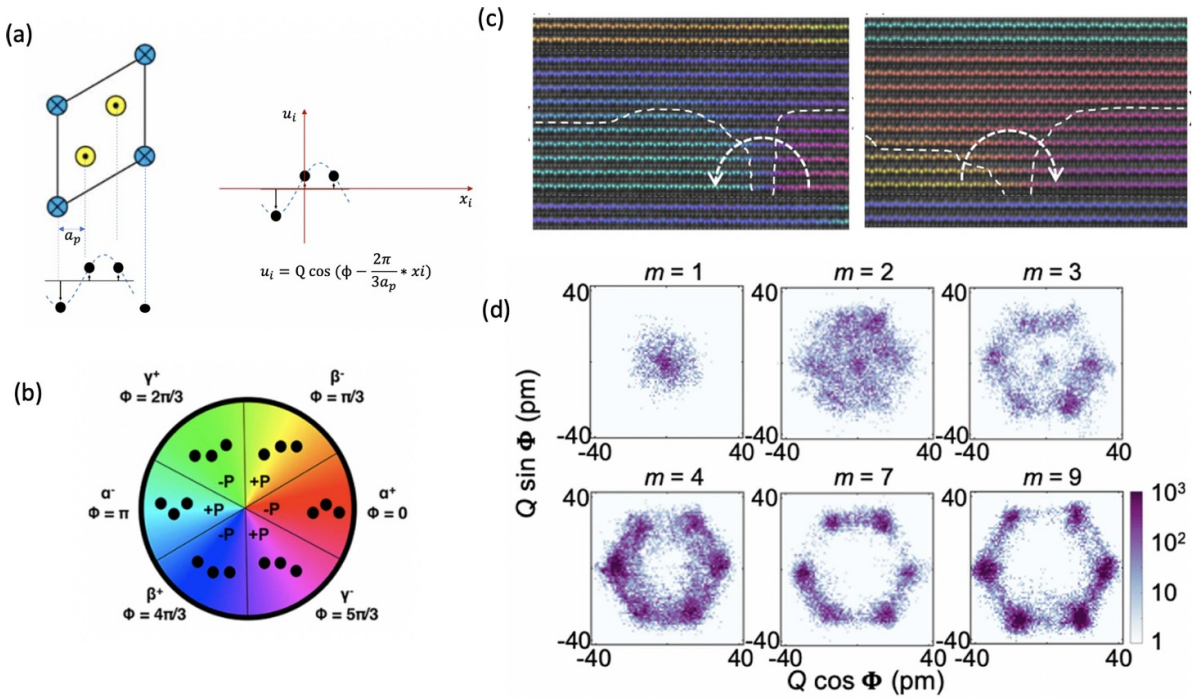

Figure 7. (a) Schematics for the quantification of (Q', ϕ_Q), based on the positions of rare earth. (b) Patterns of rare earth with different ϕ. (c) Ferroelectric domain distribution and the overlap of ϕ_Q in $(h\text{-}LuFeO_3)_m/LuFe_2O_4$ superlattice. (d) (Q', ϕ_Q) distributions in $(h\text{-}LuFeO_3)_m/LuFe_2O_4$ superlattice with different m. (b)–(d) Reprinted figure with permission from [74], Copyright 2022 by the American Physical Society.

$$u = u_0 + Q'\cos(\phi_Q - \vec{q}\cdot\vec{r}_n) \tag{7}$$

where the amplitude of rare-earth corrugation (Q') is proportional to Q. As shown in figure 7(a), viewed along the <100> direction, the atomic position of rare earth (x_i, y_i) can be quantified from two-dimensional gaussian fitting of STEM image. Since displacement pattern of rare earth repeats every three atoms for the single domain states, the above equation can be further modified as:

$$u_i = Q'\cos\left(\phi_Q - \frac{2\pi}{3}\frac{x_i}{a_P}\right) \tag{8}$$

in which a_P is the in-plane distance between two neighboring R, u_i is the relative displacement of the R atom, with respect to average y_i of three R atoms in the unit cell. Based on the least-square fit of the R position using above equation, the order parameter (Q', ϕ_Q) can be extracted. Figure 7(b) shows the schematic patterns of three neighboring R atoms for different ferroelectric domains.

Moreover, this method can be applied to visualize ferroelectric domain distributions in real space. As shown in figure 7(c), the half-vortex is pinned at the interface in $(h\text{-}LuFeO_3)_m/(LuFe_2O_4)$ superlattices [74–76]. By varying m, the confinement of electrostatic boundary condition on the topological defects can be quantified from the distribution of the order parameters (see figure 7(d)). As the thickness of $h\text{-}LuFeO_3$ layer increases, ϕ_Q for the majority of domains is $n * \frac{\pi}{3}$ with integer n, which is consistent with the energy landscape from the Landau theory. When m decreases, an emergent P3c1 symmetry is observed for $m = 2$ before $h\text{-}LuFeO_3$ becomes paraelectric phase with $m = 1$ [74, 77]. Similar methods have also been applied to track the improper ferroelectricity near phase transition, interface, and defects [78]. These results provide an unprecedented degree of control over ferroelectric domains in hexagonal rare-earth ferrites, pushing the boundary of the fundamental understanding of improper ferroelectrics and the exploration of novel functionalities.

3. Magnetism

Beyond the improper ferroelectricity, the structural distortions also play the key role in the spin-lattice coupling by the modulating magnetic free energy [79–81], which provides the microscopic picture to understand the spin orders in h-$RFeO_3$, such as Neel temperature (T_N), net magnetization of canted antiferromagnetism, and the single-ion magnetic anisotropy.

3.1. Spin-lattice coupling in h-RFeO_3

The Fe spins associated with magnetic order of h-$RFeO_3$ are displayed in figure 8(a), which are mostly in-plane with a small canting toward the c axis, corresponding to weak ferromagnetism or canted-antiferromagnetism [29–31, 82, 83]. Within the triangular lattice of FeO_5, the in-plane angle between neighboring Fe spins is 120°, corresponding to an antiferromagnetic

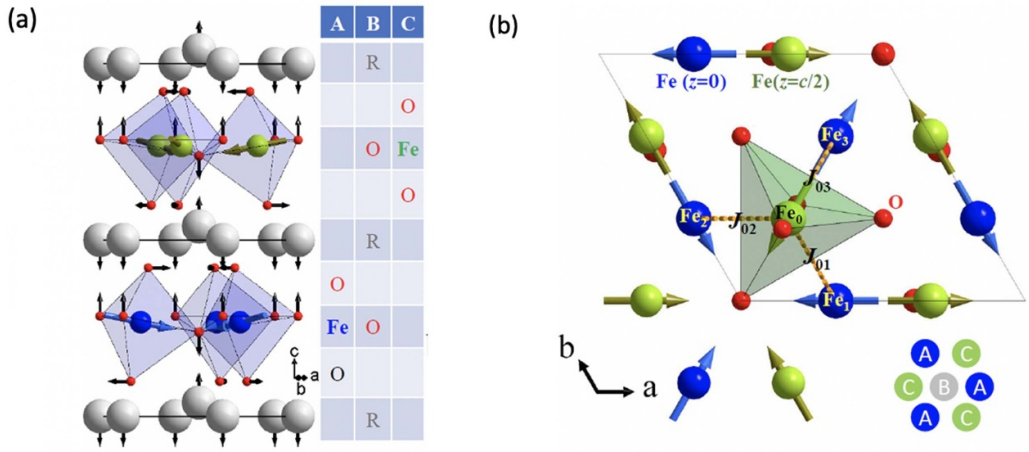

Figure 8. (a) Schematic for the canted-antiferromagnetism under the K_3 distortion in h-*R*FeO_3. (b) The top view for the alignment of Fe spins with A_2 magnetic structure and related interlayer exchange interaction. (a) and (b) Reprinted figure with permission from [30], Copyright 2018 by the American Physical Society.

order, due to a strong exchange interaction within the FeO layer.

The general expression for the effective spin Hamiltonian of a lattice is [32]:

$$\mathrm{H} = \sum_{\mathrm{ij}} J_{ij}\vec{S}_i \cdot \vec{S}_j + \sum_{\mathrm{ij}} \vec{D}_{\mathrm{ij}} \cdot \left(\vec{S}_i \times \vec{S}_j\right) + \sum_{\mathrm{i}} \vec{S}_i \cdot \overleftrightarrow{\tau}_i \cdot \vec{S}_i \quad (9)$$

in which J_{ij} is exchange interaction, $\vec{D}_{ij}$ is the DM vector, $\overleftrightarrow{\tau}_i$ is for single-ion anisotropy (SIA) tensor. Therefore, the key for understand spin-lattice coupling is to reveal how the structural distortions influence J_{ij}, $\vec{D}_{ij}$, and $\overleftrightarrow{\tau}_i$ in h-*R*FeO_3.

The effective inter-layer exchange interaction relies on the K_3 lattice distortion. For the inter-layer exchange interaction of a given Fe, there are three nearest Fe spins, as shown in figure 8(b). The K_3 distortion breaks the three-fold rotational symmetry and makes J_{03} unequal to J_{02} and J_{01}, resulting in a non-zero effective interlayer exchange energy [30]:

$$E_{\mathrm{inter}} \propto (J_{01} - J_{03})\, S(S+1) \quad (10)$$

which is expected to determine the three-dimensional ordering and the Neel temperature. Moreover, for FeO_5 bipyramids, the electronic structure of Fe is influenced by crystal field of nearby oxygen [84], which is the origin of single-ion anisotropy (SIA).

3.2. K_3 distortion and Neel temperature (T_N) in h-RFeO_3

Due to the large difference between the magnetic ordering temperature (T_N = 100–200 K) and the ferroelectric Curie temperature ($Tc \approx 1000$ K), T_N is the bottleneck to achieve room-temperature multiferroicity in single-phase h-*R*FeO_3. Since strain can modify lattice constant and resultant Fe site positions, the correlation between K_3 distortion and T_N through the strain effect has been carefully investigated [29, 30]. The K_3 distortion reduces the local symmetry of FeO_5 from C_{3v} to C_s, which leads to the interlayer exchange interaction E_{inter} in equation (10). T_N is expected to be approximately proportional to E_{inter}.

Moreover, the relationship between $J_{01} - J_{03}$ and K_3 distortion is proposed as [30, 32]:

$$J_{01} - J_{03} \propto a_2 Q_{\mathrm{K3}}^2 + a_4 Q_{\mathrm{K3}}^4 \quad (11)$$

where a_2 and a_4 are coefficients. As shown in figure 9(a), the power law relationship can be identified as:

$$\frac{T_{\mathrm{N}}}{S(S+1)} \propto Q_{\mathrm{K3}}^n \quad (12)$$

with $\mathrm{n} = 2.7 \pm 0.05$, which is consistent with the equation (11). The smaller rare earth atom is expected to reduce the in-plane lattice constant. The tolerance factor $t = (r_{\mathrm{R}} + r_{\mathrm{O}}) / \left[(r_{\mathrm{TM}} + r_{\mathrm{O}})\sqrt{2}\right]$ can also be used to gauge the K_3 structure distortion in h-*R*FeO_3. As shown in figure 9(b), by varying the rare earth atom from Er to Sc, the smaller tolerance factor corresponds to stronger K_3 distortion Correspondingly, T_N increases from 125 K for h-$ErFeO_3$ to 185 K for h-$ScFeO_3$. A similar trend of T_N also exists in h-$RMnO_3$ [85, 86]. On the other hand, the hydrostatic pressure could also modulate *c*/*a* ratio and the K_3 distortion, the relationship between the *c*/*a* ratio and the tilt angle of FeO_5 bipyramids is given in the inset of figure 9(c). With the increase of hydrostatic pressure, the enhanced K_3 distortion leads to the increase of T_N for $Lu_{0.5}Sc_{0.5}FeO_3$ [60]. Moreover, the electron doping for R site or ion doping in Fe site may also modify the magnetization [87, 88].

3.3. K_3 distortion and weak ferromagnetism in h-RFeO_3

The net magnetization along the *c* axis is proportional to the canted angle of Fe spins, which originates from the competition between the intralayer exchange interaction and the DM interaction [89–91]. As shown in figure 10(a), the K_3 structural distortion causes a displacement of oxygen atom at center (δ)

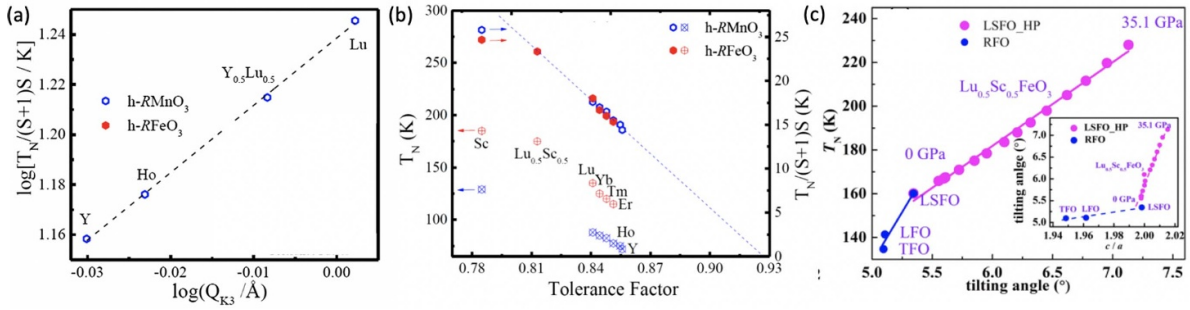

Figure 9. (a) $\log\left[T_N/\left(S+1\right)S/K\right]$ as a function of $\log\left(Q\right)$. (b) The dependence of T_N on tolerance factor. (c) The pressure-dependent tilting angle of FeO_5 and T_N. (a) and (b) Reprinted figure with permission from [30], Copyright 2018 by the American Physical Society. (c) Reprinted figure with permission from [60], Copyright 2019 by the American Physical Society.

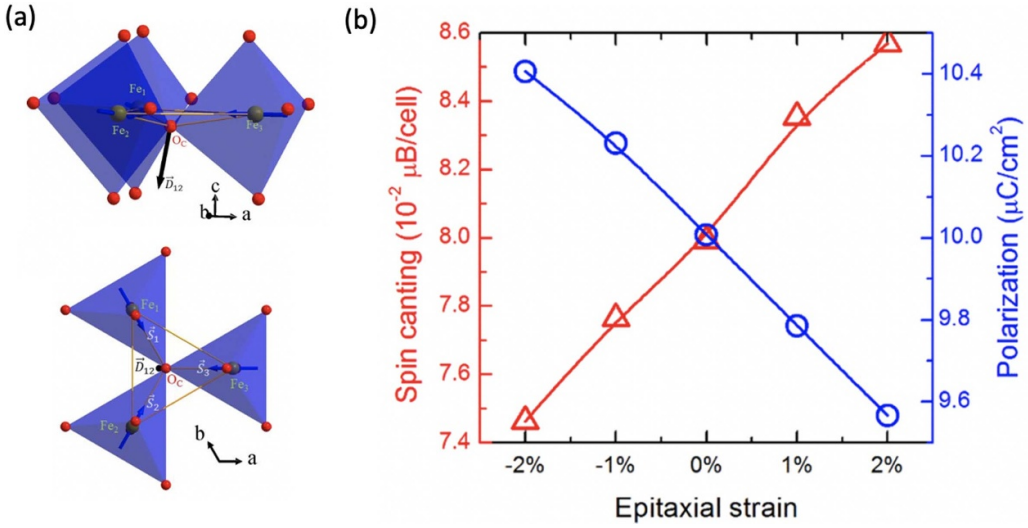

Figure 10. (a) Schematics of FeO_5 trimer from side view and top view. (b) The epitaxial strain-dependent net magnetic moment and polarization in h-$R$$FeO_3$, using DFT. (a) Reprinted figure with permission from [30], Copyright 2018 by the American Physical Society. (b) Reprinted figure with permission from [59], Copyright 2017 by the American Physical Society.

along the c axis. The vector coefficient of DM interaction ($\vec{D}_{12}$) for neighboring Fe_1 and Fe_2 is perpendicular to the Fe_1-Oc-Fe_2 plane, corresponding to a direction along

$$\left(\frac{a\delta}{\sqrt{3}}, 0, \frac{\sqrt{3}a^2}{18}\right), \tag{13}$$

where a is the in-plane lattice constant. This direction can be represented by a small tilt angle ϕ_{DM} away from the c axis with $\tan\left(\phi_{\mathrm{DM}}\right) = \frac{6\delta}{a}$. The magnitude of the DM interaction follows $D \propto a^2$ approximately because $\delta \ll a$. By minimizing the total energy of exchange interaction and DM interaction, the canting angle of Fe spin follows:

$$\theta_{\mathrm{cant}} \approx \frac{D}{\sqrt{3}J}\phi_{\mathrm{DM}} \propto \frac{a^2\phi_{\mathrm{DM}}}{J}. \tag{14}$$

The above model indicates that the in-plane compressive strain cannot decide the net magnetic moment directly. The smaller in-plane lattice constant (a) is expected to reduce the DM interaction (because $D \propto a^2$) and enhance the exchange interaction J, which decreases θ_{cant}. On the other hand, smaller a can enhance the K_3 distortion and the tilt angle ϕ_{DM}, which increases θ_{cant}. Experimentally, by selecting the rare earth with different atomic radius, it is shown that a reduced a actually leads to a smaller net magnetic moment [30], suggesting that the strain effect on the DM and exchange interactions dominates. Figure 10(b) demonstrates the relationship between the spin canting and the in-plane epitaxial strain calculated by DFT [59], which is consistent with the experiments qualitatively. Therefore, the unexpected reduction of net magnetic moment under compressive strain in h-$R$$FeO_3$ can be understood based on spin-lattice coupling that has a strong effect on the DM interaction.

3.4. Effect of structure distortion of FeO_5 on single-ion anisotropy

In h-$R$$FeO_3$, the reversal of weak ferromagnetic moments along the c axis is equivalent to the rotation of the spins by 180° within the basal plane, according to the single-ion magnetic anisotropy. When Fe is displaced with respect to O in FeO_5 bipyramids (see figure 11(a)), the symmetry of FeO_5 bipyramids reduces from D_{3h} to Cs, leading to a

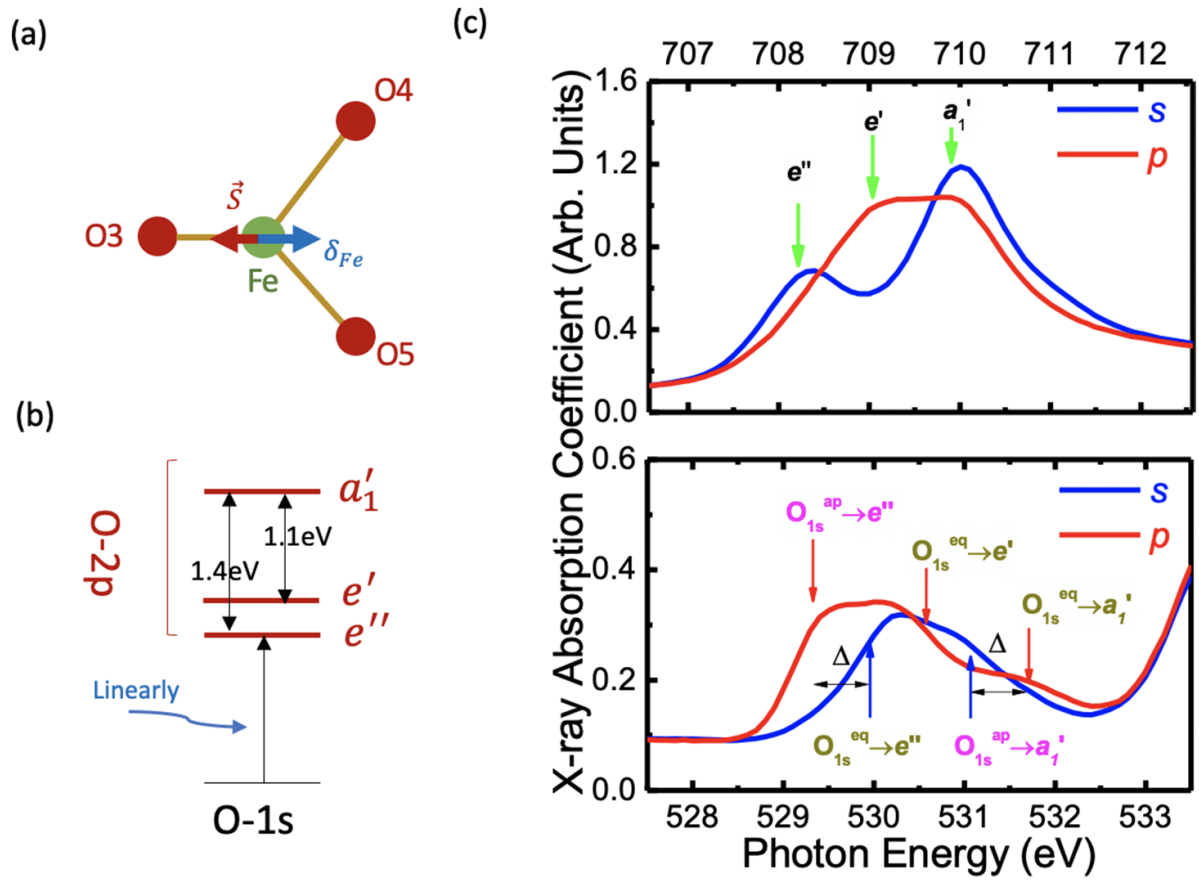

Figure 11. (a) Schematics of K_1 mode distortion within FeO_5. (b) Schematic for the XAS of O K edge and (d) related experimental XAS spectra in h-$LuFeO_3$ for Fe L_3 edge and O K edge.

single-ion magnetic anisotropy via spin-lattice coupling. The one-electron Hamiltonian to describe the single-ion magnetic anisotropy can be written as [43]:

$$H_\alpha = V_{\mathrm{CF}}(d) + \xi \vec{L}\cdot\vec{S} - J\vec{S}\cdot\hat{\alpha} \tag{15}$$

where the first term is the energy of Fe electrons in the crystal field, which depends on the perturbation parameter d that is proportional to structural distortion of FeO_5 bipyramids ($d \propto -\delta_{Fe}$). The second term is the spin-orbital coupling term and the third term represents molecular field on the Fe spin. The single-ion anisotropy energy can be found from the dependence of total energy on direction $\hat{\alpha}$, with $\hat{\alpha} = \hat{x}, \hat{y}, \hat{z}$, and the anisotropy energy is lower in the x direction ($E_x - E_z < E_y - E_z$) for $\delta_{Fe} > 0$ [43].

For h-$RFeO_3$, one electron picture has been used to interpret the x-ray absorption spectroscopy (XAS) of oxygen-K edge [92, 93], since the energy of unoccupied oxygen p states is determined by their hybridization with the Fe 3d states (see figure 11(c)). By analyzing the XAS spectra for both Fe L_3 and O K edge, the hybridization between Fe 3d and O 2p can be verified. (see figure 11(c)). The experimental evidence of hybridization and crystal-field splitting provides critical parameters in equation (15) to decide the single-ion anisotropy due to the K_1 distortion.

3.5. *The ferrimagnetic order in h-YbFeO$_3$*

When R sites are occupied by magnetic ions, such as Yb^{3+}, the interplay between the R sublattice and Fe sublattice leads to ferrimagnetic order due to the difference in magnitude of the R and Fe spins [94–96]. A schematic of spin arrangement for Yb and Fe sites are depicted in figure 12(a), where the net magnetic moment of the Yb layer is antiparallel with the net magnetic moments of the Fe layer. According to the mean-field theory [97–99], the magnetization of Yb can be approximated as:

$$M_{Yb} = \mu_{Yb}^2 \frac{\Gamma_{YbFe}\, M_{Fe} + \mu_0 H}{3k_B T} \tag{16}$$

where μ_{Yb} is the magnetic moment of Yb, Γ_{YbFe} is the molecular field parameters for Yb-Fe interaction, H is the magnetic field, M_{Fe} is the magnetization of the Fe sublattice, T is temperature, μ_0 and k_{B} are vacuum permeability and Boltzmann constants, respectively. As shown in figure 12(b), the x-ray magnetic circular dichroism (XMCD) contrast of Yb M_5 edge shows a linear dependence at high field. According to equation (16), the slope for the field dependence is $\chi_{\mathrm{Yb}} = \frac{\mu_{\mathrm{Yb}}^2 \mu_0 H}{3k_{\mathrm{B}}T}$, from which one can calculate $\mu_{Yb} = 1.6 \pm 0.1\ \mu_B$, which is significantly reduced with respect to the magnetic moment of free Yb (4.5 μ_{B}). The reduced value of μ_{Yb} can

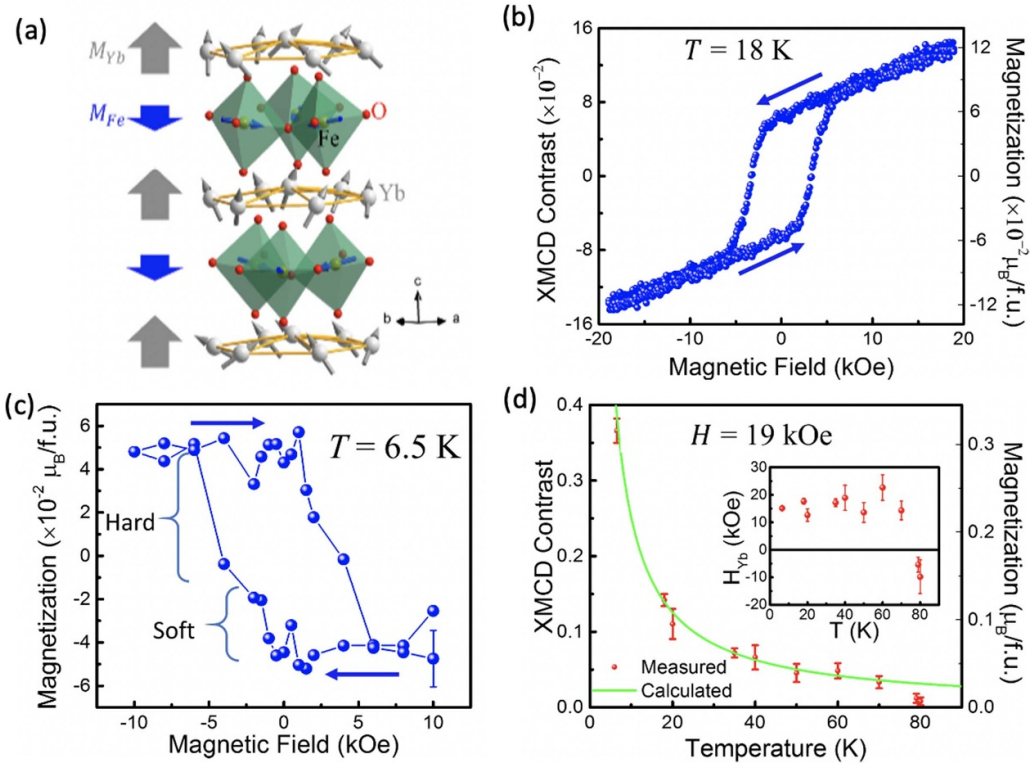

Figure 12. (a) Schematics for the spin configuration in h-$YbFeO_3$. (b) The magnetic field-dependent XMCD contrast for Yb M_5 edge and related magnetic moment of Yb. (c) Magnetic field dependence of the magnetization of Fe at 6.5 K. (d) The temperature dependence of XMCD contrast for Yb M_5 edge. (a)–(d) Reprinted figure with permission from [94], Copyright 2017 by the American Physical Society.

be attributed to the excitation of the 4*f* electrons in Yb to low-lying crystal-field states. The hysteresis of Fe magnetization shows a reversed field-dependence (see figure 12(c)), indicating that M_{Fe} and M_{Yb} have different sign in the zero field, corresponding to the ferrimagnetic orders and $\Gamma_{YbFe} < 0$. The similar magnetic coercive fields for Fe and Yb also indicate that the exchange field on Yb is generated by the Fe sites.

When temperature is much lower than the magnetic ordering temperature (≈120 K for h-$YbFeO_3$), M_{Fe} can be treated as constant of the saturation value. Combining the measured M_{Yb} in fixed magnetic field (∼19 kOe) at different temperature, the exchange field on Yb (H_{Yb}) can be calculated using equation (17). The result is $H_{Yb} \approx 17$ kOe at low temperature (see inset of figure 12(d)). H_{Yb} changes sign at about 80 K, indicating a possible realignment between the magnetization M_{Fe} and the external field.

3.6. Magnetic domains in h-RFeO_3

Magnetic anisotropy in h-*R*FeO_3 is uniaxial because the net magnetic moment comes from the canted antiferromagnetism along the *c* axis. The small net magnetization results in small magnetostatic energy and large magnetic domains. However, when the *R* sites are magnetic, like in h-$YbFeO_3$, the larger magnetization and larger magnetostatic energy reduce the domain size. Magnetic domains in h-*R*FeO_3 films with and without ferrimagnetic order have been investigated using magnetic force microscopy (MFM) at cryogenic temperature [58, 100].

Figures 13(a)–(l) show the MFM images at 6 K after zero field cooling (ZFC) for a 200 nm-thick h-$LuFeO_3$/YSZ (111) film [58], in which the magnetization only comes from the Fe spins. The labyrinth-like virgin domain state, with the domain size of ∼1.8 μm, is identified at zero field (figure 13(a)). The domain wall starts moving when the magnetic field reaches about 3.5 T. With increasing the magnetic field, the magnetization saturates at 5 T. The magnitude of magnetization remains constant when the field is decreased from 5 T to 0 T, indicating a perpendicular magnetic anisotropy. As the magnetic field is changed from −3 T to −3.2 T, the up domain is reversed via domain nucleation and domain wall propagation. Figure 13(m) shows the *M-H* curve deduced from the MFM images, indicating that the h-$LuFeO_3$ is a hard ferromagnet. Moreover, the temperature-dependent MFM images exhibit that the domain contrast becomes weaker with increasing temperature, following a mean-field-like behavior with $T_c \approx 148$ K. For h-$YbFeO_3$, a much smaller magnetic domain size on the order of several hundred nanometers was observed [100], due to the stronger magnetostatic contribution from Yb, as shown in figure 13(n). The enhanced domain contrast can be attributed to nucleation of magnetic domains when the magnetic field is close to the magnetic coercive filed (approximately ±4000 Oe).

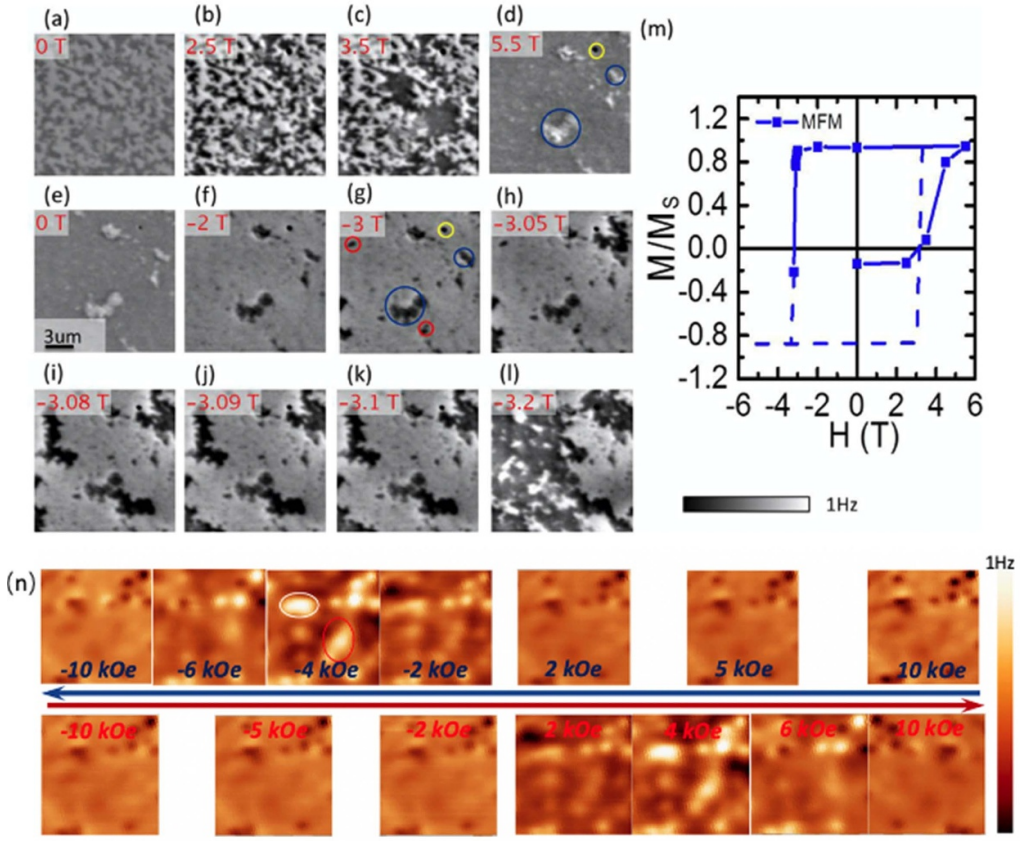

Figure 13. (a)–(l) MFM images of 200 nm-thick h-$LuFeO_3$/YSZ (111) film measured under different magnetic field after ZFC. (m) The *M-H* curve extracted from the MFM images from (a) to (l). (n) MFM images of h-$YbFeO_3$/YSZ (111) film under different magnetic field, the scan size is 3*3 μm. (a)–(m) Reprinted figure with permission from [58], Copyright 2017 by the American Physical Society. (n) Reproduced from [100]. CC BY 4.0.

4. Magnetoelectric couplings

In single-phase multiferroic h-*R*FeO_3, the improper nature of ferroelectricity as well as the spin-lattice coupling imply that the structural distortions may serve as the bridge for the interplay between spin order and electrical polar order, leading to a magnetoelectric (ME) coupling [29–32, 101–103]. Due to the existence of domains as well as domain walls for both ferroelectricity and magnetism, the ME coupling in h-*R*FeO_3 can be divided into the bulk-state ME coupling as well as domain-wall ME coupling.

4.1. Magnetoelectric coupling in bulk-state

For bulk or single domain state h-*R*FeO_3, we describe the spin direction of Fe and the apical displacement of FeO_5 (from the K_3 distortion) using ϕ_L and ϕ_Q respectively. The net magnetization (M) can be described as [50]:

$$M = -M_S \cos\left(\phi_Q - \phi_L\right). \tag{17}$$

Figure 14(a) gives the correlation of polarization (*P*) and *M* in triangle-bipyramids of h-$RFeO_3$. As shown in figure 14(b), under the external electric field, the switching of polarization direction is accompanied by a rotation of ϕ_Q by 60°. If ϕ_L does not follow the change of ϕ_Q, the magnetization direction would reverse, corresponding to the ME coupling for the bulk-state. Otherwise, if ϕ_L follows ϕ_Q, the direction of magnetization will not change, corresponding to the ME decoupling. The energy landscape in (ϕ_Q, ϕ_L) space is given in figure 14(c), where the energy barrier is higher on the path of the ME coupling. Therefore, when the polarization is switched by the electric field, the net magnetization is expected to be decoupled from it.

Experimentally, for h-$Lu_{0.5}S_{0.5}cFeO_3$ single crystals [104], the size of the magnetic domains is on the order of 100 μm, while the size of the ferroelectric domain is on the order of 1 μm. No identifiable correlations between the magnetic and ferroelectric domains can be observed experimentally. The large domain-size mismatch also suggests the ME decoupling, as shown in figure 14(d). Therefore, the bulk-state ME coupling previously predicted [32], in which the magnetization switching follows with the polarization switching at the ferroelectric vortex under external electric filed, as illustrated in figure 14(e), may not be the most possible scenario in h-*R*FeO_3.

Here, we briefly comparing h-$RFeO_3$ with the other widely studied multiferroics, $BiFeO_3$. The bulk-state magnetoelectric

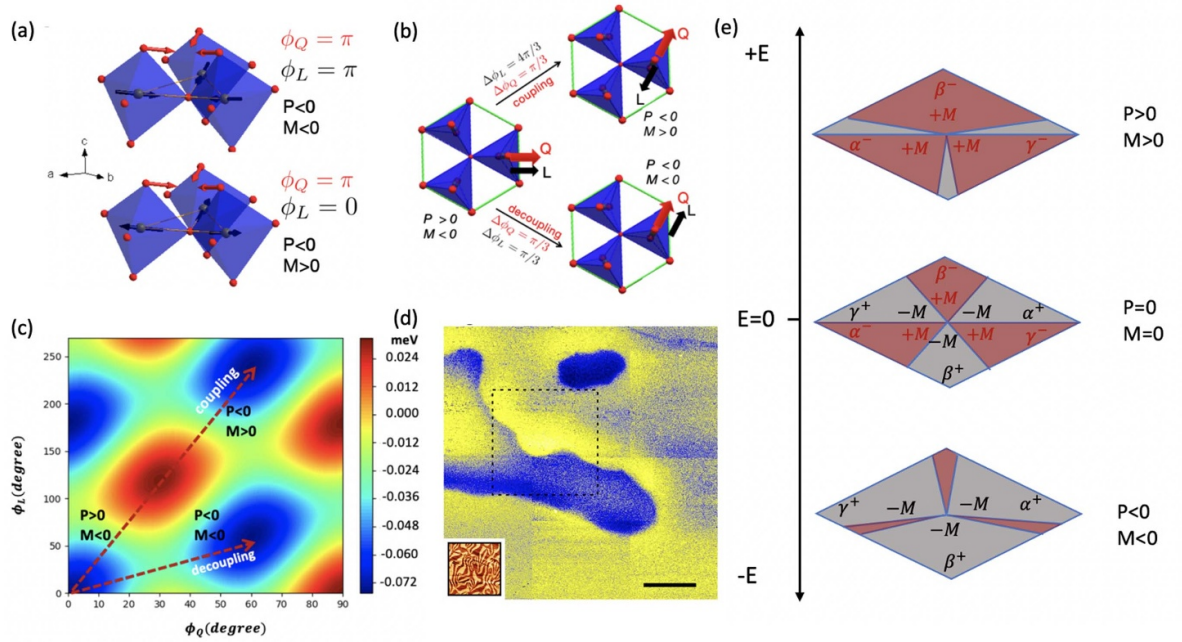

Figure 14. (a) Schematic for the spin direction (ϕ_L) and structural distortion (ϕ_Q) within the triangle lattice of FeO_5 bipyramids. (b) Schematic for the ME coupling and decoupling when the polarization is switched from $P > 0$ to $P < 0$. (c) The energy landscape in (ϕ_Q, ϕ_L) space. (d) MFM image of the h-$Lu_{0.5}Sc_{0.5}FeO_3$, the inset is the PFM phase image. (e) Proposed ME coupling at ferroelectric vortex. (a)–(c) Reproduced from [100]. CC BY 4.0. (d) Reproduced from [104]. CC BY 4.0.

coupling in single-phase $BiFeO_3$ hinges on the rotation of magnetic easy plane associating with the 71° or 109° rotation of polarization, which along the <111> direction in pseudo-cubic structure [11, 105]. Due to the polarization of h-$RFeO_3$ can only be switched along *c*-axis, as well as the high-energy barrier on switching path ME coupling, the forbidden electric field-driven magnetization switching in h-$RFeO_3$ resembles the similar forbidden behavior in $BiFeO_3$ during 180° polarization switching.

On the other hand, the heterostructures of ferromagnet on $BiFeO_3$ indicate the change of antiferromagnetic easy plane during polarization switching can also couple with neighboring ferromagnetic layers, achieving the strong ME coupling in composite form [106, 107]. For h-$RFeO_3$, the known explored magnetic layer is $LuFe_2O_4$ and inverse-spinel $CoFe_2O_4$. The magnetic Curie temperature is enhanced for the former [75]. The magnetic properties $CoFe_2O_4$ layer is still less explored, the potential electric-field driven change of exchange bias may rely on the interfacial monolayer reconstruction [108].

4.2. Magnetoelectric coupling in clamped antiferromagnetic domain wall

Despite the bulk-state ME decoupling, the ferroelectric domain walls of h-*R*FeO_3 could support the ME coupling [109, 110]. As shown in figure 15(a), the FE domain wall of h-*R*FeO_3 is defined by a sharp change of ϕ_Q [26, 110], which induces the change of ϕ_L due to the single-ion magnetic anisotropy, corresponding to the so-called clamped antiferromagnetic (AFM) domain wall [48]. The magnitude of the magnetization decreases within the clamped AFM domain wall. Moreover, the relatively smaller domain-wall energy in h-*R*FeO_3 suggests the possibility of large population of ferroelectric domain walls. By changing electrostatic conditions or grain size in h-*R*FeO_3 thin films, the population of FE domain walls can be tuned [111, 112] and then influences the distribution of clamped AFM walls (see figures 15(b) and (c)). Due to the appearance of FE domain walls, ϕ_L cannot follow the change of ϕ_Q, and thus the net magnetization will be suppressed as the FE domain-wall density increases, as shown in figure 15(c). In other words, by controlling the density of FE walls during the ferroelectric switching, the magnitude of the magnetization can be changed, which provides a new ME coupling mechanism linked with ferroelectric and magnetic domain walls.

Experimentally, the polarization switching has been achieved in h-$YbFeO_3$/CFO/LSMO thin films [52], as shown in figure 15(d). Blocks 1 and 3 correspond to up and down polarization, while blocks 2 and 4 correspond to zero polarization when the density of FE domain walls is expected to be maximum. Based on the *in-situ* measurement of XMCD contrast of Yb M5 edge during ferroelectric switching (see figure 15(e)), the lower XMCD contrasts in blocks 2 and 4, compared with that of the blocks 1 and 3, substantiate the domain-wall ME coupling discussed above. The critical condition for achieving the domain-wall ME coupling is that the

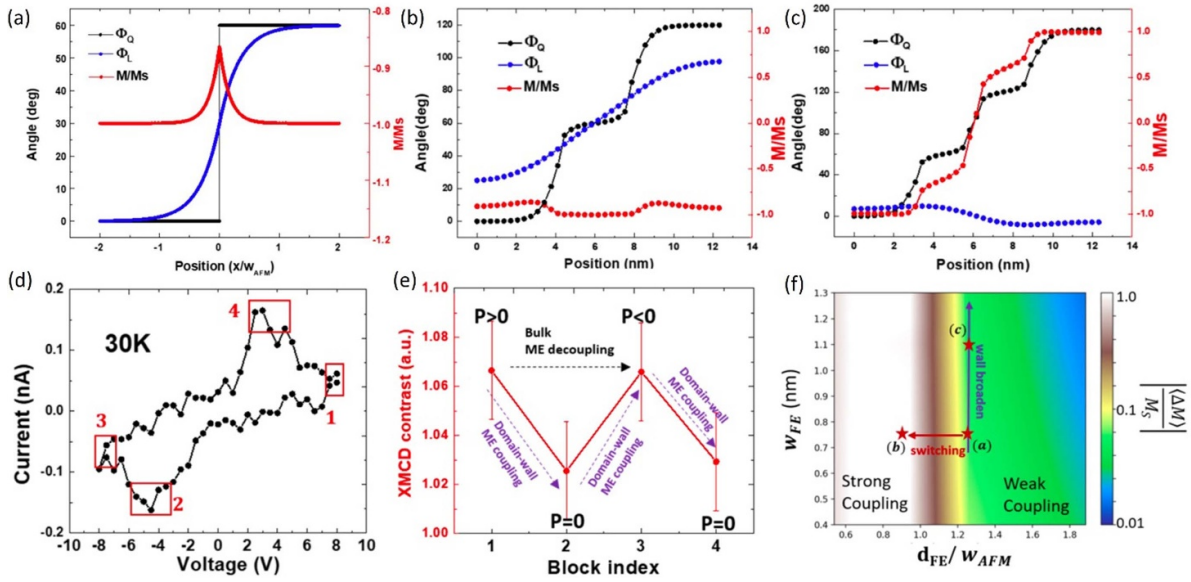

Figure 15. (a) Schematic for the single clamped antiferromagnetic (AFM) domain wall in h-$YbFeO_3$. Clamped AFM wall for 12 nm-diameter grains with (b) two and (c) three uniformly distributed ferroelectric domain walls. (d) The voltage-dependent switching current for h-$YbFeO_3$ thin films at 30 K. (e) The XMCD contrast of Yb M_5 edge for different blocks. (f) Phase diagram of average magnetization reduction due to domain-wall ME coupling, with respect to w_{FE} and d_{FE}/w_{AFM}. (a)–(f) Reproduced from [100]. CC BY 4.0.

FE domain size (d_{FE}) is smaller than the width of the AFM domain wall (w_{AFM}), as shown in figure 15(f).

5. Outlook and summary

During the past decades, substantial progresses have been made on atomic-scale synthesis control, high-precision characterization, and multiscale material modeling on hexagonal rare-earth ferrites. This boosts the physic understanding of their fundamental multiferroic properties, particularly the role of non-polar structure distortion on ferroelectricity, magnetism, and ME couplings. The improper ferroelectricity and spin-lattice coupling have been revealed as the origin of the abundant multiferroic properties in h-$R$$FeO_3$, as shown in figure 16, which is expected to stimulate the fresh ideas for the non-perovskite-structure multiferroics, including but not limiting to:

1. The improper ferroelectric h-$R$$FeO_3$, compared with their proper perovskite counterparts [113, 114], exhibits exotic functionalities, including the dominating role of non-polar structural K_3 distortion on ferroic orders, smaller domain wall energy, and the absence of critical thickness. The removal of interfacial clamping (see section 2.3) would make h-$RFeO_3$ ferroelectric with 1 nanometer thickness, comparable to two-dimensional ferroelectrics.
2. For magnetism, T_N and weak ferromagnetism are determined by the K_3 distortion, while the single-ion anisotropy hinges on the K_1 distortion. So, methods that can modulate atomic-scale structural distortion, such as chemical doping and hydrostatic pressure, can be effective in further tuning the magnetic properties.
3. Although the bulk-state ME coupling is not favored, the reduced symmetry at the ferroelectric domain walls enables the macroscopic identification for domain-wall ME coupling at nanoscale, which was observed during ferroelectric switching. Hence, ME coupling could be explored in local, low symmetry configurations.
4. Hexagonal rare-earth ferrites h-$RFeO_3$ can serve as robust ultrathin ferroelectric template to induce potential proximity-like effect in neighboring materials, such as enhancement of T_c in $LuFe_2O_4$ [75] and enhancement of spin-Hall angle in heavy metal by the Rashba-Edelstein effect (REE) [115], or control of magnetic skyrmions [87].

Some challenges about multiferroic h-$R$$FeO_3$, however, remain to be addressed in the future, calling for concerted efforts and advanced capabilities in thin-film synthesis, characterization, and modeling. We summarize several challenges and perspectives as follows:

From the perspective of improper ferroelectricity, the demonstration of absence of critical thickness in h-$R$$FeO_3$ has been hindered by the 'practical' critical thickness, i.e. the suppression of the K_3 distortion at the film/substrate interface due to the structural clamping effect. Other factors, such as oxygen-off stoichiometry [116], interfacial reconstruction [117], should be further clarified, in order to make h-$RFeO_3$ scale-free ferroelectric materials experimentally. Moreover, novel electric properties of h-$R$$FeO_3$ are much less explored. For example, the multi-parameter energy diagram and the resulting complex polarization switching path of h-$R$$FeO_3$ may lead to non-traditional polarization-voltage relation under different restrictions [72]. In particular, due to the nature of improper ferroelectricity, the charged domain walls are prevalent [74, 110], which may exhibit distinguished electrical

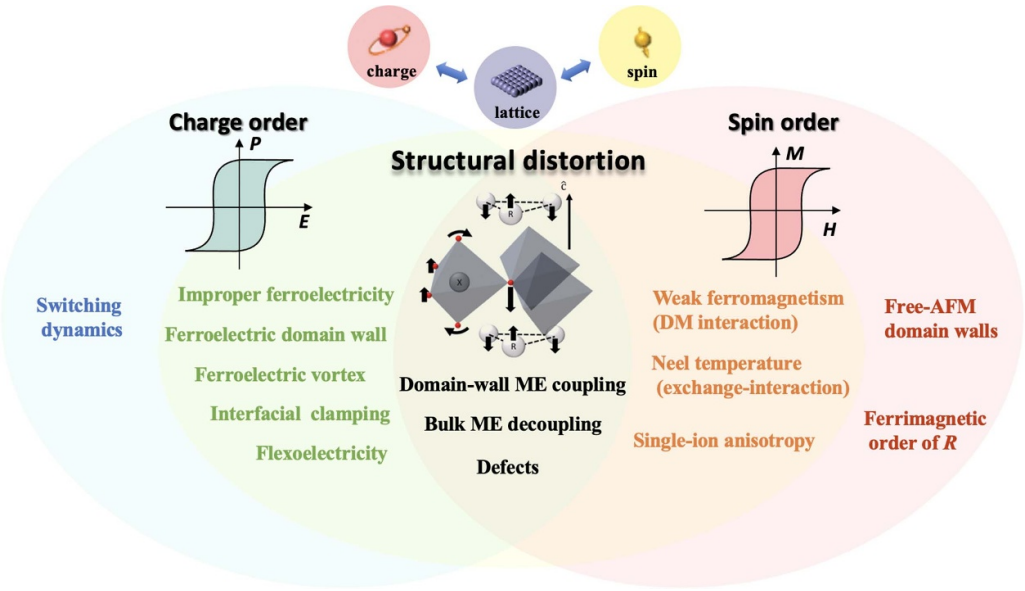

Figure 16. The global view of the relation between spin, charge, and lattice of h-$RFeO_3$ representing current understandings.

performance, in concert with hexagonal structure. The unique response of K_3 structural distortion to strain may offer novel mechanism of coupling strain gradient and polarization, i.e. flexoelectricity [118–120]. To address these issues, the synthesis of high-quality hexagonal rare-earth ferrites films is of particular importance. Nevertheless, this is still restricted by the availability of substrates and appropriate electrodes. Expanding the range of available conducting substrates with matching structures is a key step. In turn, for magnetism, questions remain on how to increase T_N of single-phase h-$RFeO_3$ film above room temperature, by e.g. chemical doping, epitaxial strain.

Besides the 'bulk' state properties, local topological phenomena in h-$RFeO_3$ are also important in future research directions. A good example is the famous six-fold ferroelectric vortex which has been demonstrated in single crystal samples as a topological defect with a micrometer scale, accompanied by collective scaling behavior [121–125]. On a smaller scale, screw dislocations, which are often observed in hexagonal materials [126–128], can introduce stronger modulation to the multiferroic properties, and generate topological phenomenon like polar and magnetic skyrmions in h-$RFeO_3$ films [129–131].

Regarding substrate clamping effects and limited flexibility, a promising mean to expand strain control is to release freestanding membranes from the substrates and transfer them to various substrates. For example, the compatibility of h-$RFeO_3$ on classic perovskite-structure bottom electrode layer, such as h-$ScFeO_3$ on $La_{0.67}Sr_{0.33}MnO_3$ (LSMO) /$SrTiO_3$(111), as well as atomic-scale synthesis control through *in-situ* monitoring of RHEED, provide an opportunity to achieve freestanding h-$RFeO_3$ by dissolving LSMO layer or inserting solvable buffer layer [132, 133]. This holds great promise for a larger degree of control over ferroic orders and thus realizing profuse novel phenomena. In addition, the removal of interfacial clamping in h-$RFeO_3$ may enhance the polarization state with the thickness as low as monolayer [134–136], due to the improper nature of ferroelectricity.

On application level, the improper ferroelectricity of h-$RFeO_3$ shows the great advantages in non-volatile ferroelectric memory devices, such as ferroelectric capacitor, FeRAM, FeFET, which all hinges on the maintenance of remnant polarization after removing electric field [137–139]. Moreover, the thickness-dependent coercivity basically follows the JKD-scaling with $Ec \sim t^{-2/3}$ down to $\sim$ 5 nm or even thinner [52], indicating the continuous decrease of coercive volage with shrinking the thickness, which is beneficial for the energy efficiency. Meanwhile, the polarization could maintain above 2 uC cm^{-2} in ultrathin film. On the other hand, the improper nature of h-$RFeO_3$ could also help verify the generality of proposed mechanism and application, based on polarization switching in proper ferroelectrics, such as negative capacitance [72]. However, for the real application of h-$RFeO_3$ as ferroelectrics, it still needs to overcome compatibility problem with known semiconductor materials, such as Si, which is less explored to our best knowledge. The domain wall of h-$RFeO_3$ is similar to the isomorphic h-$RMnO_3$, related anisotropic conductance makes domain walls themself as the electronic components [140]. Recently, the enhanced photovoltaic efficiency in h-$RFeO_3$ films via strain engineering also indicates the application potential for photovoltaics devices [141].

Overall, the abundance of emerging phenomena in h-$RFeO_3$ have been connected via the complex crystal structure and the spin-lattice coupling one after another. At this point, hexagonal rare-earth ferrites are poised to be exploited for applications in terms of their advantageous electric properties associated with the improper ferroelectricity, particularly in the ultrathin films. In addition, exploring their local topological polar and magnetic properties will be intriguing to understand quantum phenomena in complex materials. We hope that this progress review article may inspire further investigations

into hexagonal rare-earth ferrites and their potential applications in future electronics.

Data availability statement

No new data were created or analysed in this study.

Acknowledgment

The authors acknowledge the primary support from the National Science Foundation (NSF) through EPSCoR RII Track-1: Emergent Quantum Materials and Technologies (EQUATE), Award No. OIA-2044049. The work was also supported in part by the Nebraska Center for Energy Sciences Research (NCESR).

ORCID iDs

Xin Li https://orcid.org/0000-0002-7996-8430
Yu Yun https://orcid.org/0000-0002-4893-7156
Xiaoshan Xu https://orcid.org/0000-0002-4363-392X

References

[1] Fiebig M, Lottermoser T, Meier D and Trassin M 2016 The evolution of multiferroics *Nat. Rev. Mater.* **1** 16046
[2] Lu C, Wu M, Lin L and Liu J-M 2019 Single-phase multiferroics: new materials, phenomena, and physics *Natl Sci. Rev.* **6** 653–68
[3] Salje E K H 2012 Ferroelastic materials *Annu. Rev. Mater. Res.* **42** 1.1–1.19
[4] Dawber M, Rabe K M and Scott J F 2005 Physics of thin-film ferroelectric oxides *Rev. Mod. Phys.* **77** 1083
[5] Ramesh R and Spaldin N 2007 Multiferroics: progress and prospects in thin films *Nat. Mater.* **6** 21–29
[6] Hill N A 2000 Why are there so few magnetic ferroelectrics ? *J. Phys. Chem.* B **104** 6694–709
[7] Spaldin N A and Ramesh R 2019 Advances in magnetoelectric multiferroics *Nat. Mater.* **18** 203–12
[8] Fiebig M 2005 Revival of the magnetoelectric effect *J. Phys. D: Appl. Phys.* **38** R123
[9] Scott J 2013 Room-temperature multiferroic magnetoelectrics *NPG Asia Mater.* **5** e72
[10] Eerenstein W, Mathur N and Scott J 2006 Multiferroic and magnetoelectric materials *Nature* **442** 759–65
[11] Wang J *et al* 2003 Epitaxial $BiFeO_3$ multiferroic thin film heterostructures *Science* **299** 1719–22
[12] Fiebig M, Lottermoser T, Fröhlich D, Goltsev A V and Pisarev R V 2002 Observation of coupled magnetic and electric domains *Nature* **419** 818–20
[13] Valencia S *et al* 2011 Interface-induced room-temperature multiferroicity in $BaTiO_3$ *Nat. Mater.* **10** 753–8
[14] Gruverman A, Wu D, Fan H-J, Vrejoiu I, Alexe M, Harrison R J and Scott J F 2008 Vortex ferroelectric domains *J. Phys.: Condens. Matter* **20** 342201
[15] Balke N *et al* 2012 Enhanced electric conductivity at ferroelectric vortex cores in $BiFeO_3$ *Nat. Phys.* **8** 81–88
[16] Das S *et al* 2019 Observation of room-temperature polar skyrmions *Nature* **568** 368–72
[17] Meier D, Seidel J, Cano A, Delaney K, Kumagai Y, Mostovoy M, Spaldin N A, Ramesh R and Fiebig M 2012 Anisotropic conductance at improper ferroelectric domain walls *Nat. Mater.* **11** 284–8
[18] Mundy J *et al* 2017 Functional electronic inversion layers at ferroelectric domain walls *Nat. Mater.* **16** 622–7
[19] Meier D 2015 Functional domain walls in multiferroics *J. Phys.: Condens. Matter* **27** 463003
[20] Seidel J *et al* 2010 Domain wall conductivity in la-doped $BiFeO_3$ *Phys. Rev. Lett.* **105** 197603
[21] Lawes G and Srinivasan G 2011 Introduction to magnetoelectric coupling and multiferroic films *J. Phys. D: Appl. Phys.* **44** 243001
[22] Martin L and Rappe A 2017 Thin-film ferroelectric materials and their applications *Nat. Rev. Mater.* **2** 16087
[23] Martin L W and Crane S P 2008 Multiferroics and magnetoelectrics: thin films and nanostructures *J. Phys.: Condens. Matter* **20** 434220
[24] Trassin M 2016 Low energy consumption spintronics using multiferroic heterostructures *J. Phys.: Condens. Matter* **28** 033001
[25] Khomskii D 2009 Classifying multiferroics: mechanisms and effects *Physics* **2** 20
[26] Choi T, Horibe Y, Yi H, Choi Y J, Wu W and Cheong S-W 2010 Insulating interlocked ferroelectric and structural antiphase domain walls in multiferroic $YMnO_3$ *Nat. Mater.* **9** 253–8
[27] Goltsev A V, Pisarev R V, Lottermoser T and Fiebig M 2003 Structure and interaction of antiferromagnetic domain walls in hexagonal $YMnO_3$ *Phys. Rev. Lett.* **90** 177204
[28] Van Aken B, Palstra T, Filippetti A and Spaldin N A 2004 The origin of ferroelectricity in magnetoelectric $YMnO_3$ *Nat. Mater.* **3** 164–70
[29] Wang W *et al* 2013 Room-temperature multiferroic hexagonal $LuFeO_3$ films *Phys. Rev. Lett.* **110** 237601
[30] Sinha K *et al* 2018 Tuning the néel temperature of hexagonal ferrites by structural distortion *Phys. Rev. Lett.* **121** 237203
[31] Disseler S M *et al* 2015 Magnetic structure and ordering of multiferroic hexagonal $LuFeO_3$ *Phys. Rev. Lett.* **114** 217602
[32] Das H, Wysocki A, Geng Y, Wu W and Fennie C J 2014 Bulk magnetoelectricity in the hexagonal manganites and ferrites *Nat. Commun.* **5** 2998
[33] Zhang Y, Si W, Jia Y, Yu P, Yu R and Zhu J 2021 Controlling strain relaxation by interface design in highly lattice-mismatched heterostructure *Nano Lett.* **21** 6867–74
[34] Nordlander J, Rossell M D, Campanini M, Fiebig M and Trassin M 2021 Inversion-symmetry engineering in layered oxide thin films *Nano Lett.* **21** 2780–5
[35] Nordlander J, Rossell M D, Campanini M, Fiebig M and Trassin M 2020 Epitaxial integration of improper ferroelectric hexagonal $YMnO_3$ thin films in heterostructures *Phys. Rev. Mater.* **4** 124403
[36] Zhang X, Yin Y, Yang S, Yang Z and Xu X 2017 Effect of interface on epitaxy and magnetism in h-$RFeO_3$/Fe_3O_4/Al_2O_3 films (R = Lu, Yb) *J. Phys.: Condens. Matter* **29** 164001
[37] Cao S, Paudel T R, Sinha K, Jiang X, Wang W, Tsymbal E Y, Xu X and Dowben P A 2015 The stability and surface termination of hexagonal $LuFeO_3$ *J. Phys.: Condens. Matter* **27** 175004
[38] Moyer J A, Misra R, Mundy J A, Brooks C M, Heron J T, Muller D A, Schlom D G and Schiffer P 2014 Intrinsic magnetic properties of hexagonal $LuFeO_3$ and the effects of nonstoichiometry *APL Mater.* **2** 012106
[39] Lonkai T, Tomuta D G, Amann U, Ihringer J, Hendrikx R W A, Többens D M and Mydosh J A 2004 Development of the high-temperature phase of hexagonal manganites *Phys. Rev.* B **69** 134108

[40] Wang H *et al* 2014 Structural and electronic origin of the magnetic structures in hexagonal $LuFeO_3$ *Phys. Rev.* B **90** 014436

[41] Lilienblum M, Lottermoser T, Manz S, Selbach S M, Cano A and Fiebig M 2015 Ferroelectricity in the multiferroic hexagonal manganites *Nat. Phys.* **11** 1070–3

[42] Levanyuk A P and Sannikov D G 1974 Improper ferroelectrics *Sov. Phys.—Usp.* **17** 199

[43] Cao S *et al* 2016 On the structural origin of the single-ion magnetic anisotropy in $LuFeO_3$ *J. Phys.: Condens. Matter* **28** 156001

[44] Xu X and Wang W 2014 Multiferroic hexagonal ferrites (h-$RFeO_3$, R = Y, Dy-Lu): a brief experimental review *Mod. Phys. Lett.* **28** 1430008

[45] Rai R C, Horvatits C, Mckenna D and Du Hart J 2019 Structural studies and physical properties of hexagonal-$YbFeO_3$ thin films *AIP Adv.* **9** 015019

[46] Nordlander J, Anderson M A, Brooks C M, Holtz M E and Mundy J A 2022 Epitaxy of hexagonal ABO_3 quantum materials *Appl. Phys. Rev.* **9** 031309

[47] Li M, Tan H and Duan W 2020 Hexagonal rare-earth manganites and ferrites: a review of improper ferroelectricity, magnetoelectric coupling, and unusual domain walls *Phys. Chem. Chem. Phys.* **22** 14415–32

[48] Fennie C J and Rabe K M 2005 Ferroelectric transition in $YMnO_3$ from first principles *Phys. Rev.* B **72** 100103(R)

[49] Li X, Yun Y and Xu X S 2023 Improper ferroelectricity in ultrathin hexagonal ferrites films *Appl. Phys. Lett.* **122** 182901

[50] Artyukhin S, Delaney K, Spaldin N and Mostovoy M 2014 Landau theory of topological defects in multiferroic hexagonal manganites *Nat. Mater.* **13** 42–49

[51] Zhang C X, Yang K L, Jia P, Lin H L, Li C F, Lin L, Yan Z B and Liu J-M 2018 Effects of temperature and electric field on order parameters in ferroelectric hexagonal manganites *J. Appl. Phys.* **123** 094102

[52] Yun Y, Buragohain P, Thind A S, Yin Y, Li X, Jiang X, Mishra R, Gruverman A and Xu X 2022 Spontaneous polarization in an ultrathin improper-ferroelectric/dielectric bilayer in a capacitor structure at cryogenic temperatures *Phys. Rev. Appl.* **18** 034071

[53] Sai N, Fennie C J and Demkov A A 2009 Absence of critical thickness in an ultrathin improper ferroelectric film *Phys. Rev. Lett.* **102** 107601

[54] Nordlander J, Campanini M, Rossell M D, Erni R, Meier Q N, Cano A, Spaldin N A, Fiebig M and Trassin M 2019 The ultrathin limit of improper ferroelectricity *Nat. Commun.* **10** 5591

[55] Fong D D, Stephenson G B, Streiffer S K, Eastman J A, Auciello O, Fuoss P H and Thompson C 2004 Ferroelectricity in Ultrathin Perovskite Films *Science* **304** 1650

[56] Junquera J and Ghosez P 2003 Critical thickness for ferroelectricity in perovskite ultrathin film *Nature* **422** 506

[57] Kim Y S *et al* 2005 Critical thickness of ultrathin ferroelectric $BaTiO_3$ films *Appl. Phys. Lett.* **86** 102907

[58] Wang. W, Mundy J A, Brooks C M, Moyer J A, Holtz M E, Muller D A, Schlom D G and Wu W 2017 Visualizing weak ferromagnetic domains in multiferroic hexagonal ferrite thin film *Phys. Rev.* B **95** 134443

[59] Sinha K *et al* 2017 Effects of biaxial strain on the improper multiferroicity in $h-LuFeO_3$ films studied using the restrained thermal expansion method *Phys. Rev.* B **95** 094110

[60] Liu F *et al* 2019 Pressure-induced large enhancement of Néel temperature and electric polarization in the hexagonal multiferroic $Lu_{0.5}Sc_{0.5}FeO_3$ *Phys. Rev.* B **100** 214408

[61] Zeches R J *et al* 2009 A strain-driven morphotropic phase boundary in $BiFeO_3$ *Science* **326** 977–80

[62] Deng S *et al* 2021 Critical role of Sc substitution in modulating ferroelectricity in multiferroic $LuFeO_3$ *Nano Lett.* **21** 6648–55

[63] Kim D H, Lee H N, Biegalski M D and Christen H M 2008 Effect of epitaxial strain on ferroelectric polarization in multiferroic $BiFeO_3$ films *Appl. Phys. Lett.* **92** 012911

[64] Xu C, Yang Y, Wang S, Duan W, Gu B and Bellaiche L 2014 Anomalous properties of hexagonal rare-earth ferrites from first principles *Phys. Rev.* B **89** 205122

[65] Ishibashi Y and Takagi Y 1971 Note on ferroelectric [33] domain switching *J. Phys. Soc. Jpn.* **31** 506

[66] Ruff A *et al* 2018 Frequency dependent polarisation switching in h-$ErMnO_3$ *Appl. Phys. Lett.* **112** 182908

[67] Cheng S, Meng Q, Han M-G, Deng S, Li X, Zhang Q, Tan G, Botton G A and Zhu Y 2019 Revealing the effects of trace oxygen vacancies on improper ferroelectric manganite with *in situ* biasing *Adv. Electron. Mater.* **5** 1800827

[68] Han M-G, Zhu Y, Wu L, Aoki T, Volkov V, Wang X, Chae S C, Oh Y S and Cheong S-W 2013 Ferroelectric switching dynamics of topological vortex domains in a hexagonal manganite *Adv. Mater.* **25** 2415–21

[69] Tagantsev A K, Stolichnov I, Setter N, Cross J S and Tsukada M 2002 Non-Kolmogorov-Avrami switching kinetics [34] in ferroelectric thin films *Phys. Rev.* B **66** 214109

[70] Ishibashi Y and Orihara H 1995 A theory of D-E hysteresis loop *Integr. Ferroelectr.* **9** 57–61

[71] Du X and Chen I-W 1997 Frequency spectra of fatigue of PZT and other ferroelectric thin films *MRS Proc.* **493** 311

[72] Li X and Yun Y Duality of switching mechanisms and transient negative capacitance in improper ferroelectrics (arXiv:2309.14639)

[73] Holtz M E *et al* 2017 Topological defects in hexagonal manganites: inner structure and emergent electrostatics *Nano Lett.* **17** 5883–90

[74] Holtz M E, Padgett E, Steinhardt R, Brooks C, Meier D, Schlom D, Muller D and Mundy J 2022 Dimensionality-induced change in topological order in multiferroic oxide superlattices *Phys. Rev. Lett.* **126** 157601

[75] Mundy J *et al* 2016 Atomically engineered ferroic layers yield a room-temperature magnetoelectric multiferroic *Nature* **537** 523–7

[76] Fan S *et al* 2020 Site-specific spectroscopic measurement of spin and charge in $(LuFeO_3)_m/(LuFe_2O_4)_1$ multiferroic superlattices *Nat. Commun.* **11** 5582

[77] Huang F-T, Wang X, Griffin S, Kumagai Y, Gindele O, Chu M-W, Horibe Y, Spaldin N and Cheong S-W 2014 Duality of topological defects in hexagonal manganites *Phys. Rev. Lett.* **113** 267602

[78] Ren G, Omprakash P, Li X, Yun Y, Thind A S, Xu X and Mishra R,Polarization pinning at an antiphase boundary in multiferroic $YbFeO_3$ (arXiv:2409.08902)

[79] Lee S *et al* 2008 Giant magneto-elastic coupling in multiferroic hexagonal manganites *Nature* **451** 805–8

[80] Tošić T N, Meier Q N and Spaldin N A 2022 Influence of the triangular Mn-O breathing mode on magnetic ordering in multiferroic hexagonal manganites *Phys. Rev. Res.* **4** 033204

[81] Chen X-B, Thi Minh Hien N, Lee D, Jang S-Y, Noh T W and Yang I-S 2011 Spin exchange interactions in hexagonal manganites $RMnO_3$ (R = Tb, Dy, Ho, Er) epitaxial thin films *Appl. Phys. Lett.* **99** 052506

[82] Solovyev I V, Valentyuk M V and Mazurenko V V 2012 $YMnO_3$ and $LuMnO_3$ from a microscopic point of view *Phys. Rev.* B **86** 054407

[83] Tang Y S *et al* 2021 Magnetic structure and multiferroicity of Sc-substituted hexagonal $YbFeO_3$ *Phys. Rev.* B **103** 174102

[84] Wang W *et al* 2012 Crystal field splitting and optical bandgap of hexagonal $LuFeO_3$ films *Appl. Phys. Lett.* **101** 241907

[85] Katsufuji T *et al* 2002 Crystal structure and magnetic properties of hexagonal $RMnO_3$(R = Y, Lu, and Sc) and the effect of doping *Phys. Rev.* B **66** 134434

[86] Park J *et al* 2010 Doping dependence of spin-lattice coupling and two-dimensional ordering in multiferroic hexagonal $Y_{1-x}Lu_xMnO_3$ ($0 \leqslant x \leqslant 1$) *Phys. Rev.* B **82** 054428

[87] Swamynadhan M J, O'Hara A, Ghosh S and Pantelides S T 2024 Engineering collinear magnetization in hexagonal $LuFeO_3$ and magnetoelectric control of skyrmions in hexagonal 2D epilayers *Adv. Funct. Mater.* **34** 2400195

[88] Van Aken B B, Bos J-W G, de Groot R A and Palstra T T M 2001 Asymmetry of electron and hole doping in $YMnO_3$ *Phys. Rev.* B **63** 125127

[89] Moriya T 1960 Anisotropic superexchange interaction and weak ferromagnetism *Phys. Rev.* **120** 91–98

[90] Dzyaloshinsky I 1958 A thermodynamic theory of "weak" ferromagnetism of antiferromagnetics *J. Phys. Chem. Solids* **4** 241

[91] Keffer F 1962 Moriya interaction and the problem of the spin arrangements in βMnS *Phys. Rev.* **126** 896

[92] Cho D-Y *et al* 2007 Ferroelectricity driven by Y *d*0-ness with rehybridization in $YMnO_3$ *Phys. Rev. Lett.* **98** 217601

[93] Cho D-Y, Oh S-J, Kim D G, Tanaka A and Park J-H 2009 Investigation of local symmetry effects on the electronic structure of manganites: hexagonal $YMnO_3$ versus orthorhombic $LaMnO_3$ *Phys. Rev.* B **79** 035116

[94] Cao S *et al* 2017 Electronic structure and direct observation of ferrimagnetism in multiferroic hexagonal $YbFeO_3$ *Phys. Rev.* B **95** 224428

[95] Antonov V N and Kukusta D A 2019 Electronic structure and x-ray magnetic circular dichroism in the multiferroic oxide *h*−$YbFeO_3$ *Phys. Rev.* B **99** 104403

[96] Jeong Y K, Lee J-H, Ahn S-J, Song S-W, Jang H M, Choi H and Scott J F2012 Structurally tailored hexagonal ferroelectricity and multiferroism in epitaxial $YbFeO_3$ thin-film heterostructures *J. Am. Chem. Soc.* **134** 1450

[97] Derkachenko V N, Kodomtseva A M, Timofeeva V A and Khokhlov V A 1974 *JEPT Lett.* **20** 104 (available at: http://jetpletters.ru/ps/1787/article_27238.pdf)

[98] Zvezdin A K and Matveev V M 1972 *Sov. Phys.-JETP* **3** 140 (available at: http://jetp.ras.ru/cgi-bin/dn/e_035_01_0140.pdf)

[99] Ashcroft N W and Mermin N D 1976 *Solid State Physics* (Holt, Rinehart and Winston)

[100] Li X *et al* 2023 Domain-wall magnetoelectric coupling in multiferroic hexagonal $YbFeO_3$ films *Sci. Rep.* **13** 1755

[101] Huang Z J, Cao Y, Sun Y Y, Xue Y Y and Chu C W 1997 Coupling between the ferroelectric and antiferromagnetic orders in $YMnO_3$ *Phys. Rev.* B **56** 2623–6

[102] Das H 2023 Coupling between improper ferroelectricity and ferrimagnetism in the hexagonal ferrite $LuFeO_3$ *Phys. Rev. Res.* **5** 013007

[103] Ye M and Vanderbilt D 2015 *Phys. Rev.* B **92** 035107

[104] Du K, Gao B, Wang Y, Xu X, Kim J, Hu R, Huang F-T and Cheong S-W 2018 Vortex ferroelectric domains, large-loop weak ferromagnetic domains, and their decoupling in hexagonal (Lu, Sc)FeO_3 *npj Quantum Mater.* **3** 33

[105] Catalan G and Scott J F 2009 Physics and applications of bismuth ferrite *Adv. Mater.* **21** 2463–85

[106] Heron J *et al* 2014 Deterministic switching of ferromagnetism at room temperature using an electric field *Nature* **516** 370–3

[107] Heron J T, Trassin M, Ashraf K, Gajek M, He Q, Yang S Y, Nikonov D E, Chu Y-H, Salahuddin S and Ramesh R 2011 Electric-field-induced magnetization reversal in a ferromagnet-multiferroic heterostructure *Phys. Rev. Lett.* **107** 217202

[108] Steinhardt R 2020 Ferroic Ferrite Films: an MBE Odyssey *PhD Thesis*

[109] Geng Y, Lee N, Choi Y J, Cheong S-W and Wu W 2012 Collective magnetism at multiferroic vortex do-main walls *Nano Lett.* **12** 6055–9

[110] Kumagai Y and Spaldin N 2013 Structural domain walls in polar hexagonal manganites *Nat. Commun.* **4** 1540

[111] Småbråten D R, Meier Q N, Skjærvø S H, Inzani K, Meier D and Selbach S M 2018 Charged domain walls in improper ferroelectric hexagonal manganites and gallates *Phys. Rev. Mater.* **2** 114405

[112] Yang K L, Zhang Y, Zheng S H, Lin L, Yan Z B, Liu J-M and Cheong S-W 2017 Electric field driven evolution of topological domain structure in hexagonal manganites *Phys. Rev.* B **96** 144103

[113] Zhong W, Vanderbilt D and Rabe K M 1995 First-principles theory of ferroelectric phase transitions for perovskites: the case of $BaTiO_3$ *Phys. Rev.* B **52** 6301

[114] Cohen R 1992 Origin of ferroelectricity in perovskite oxides *Nature* **358** 136–8

[115] Li J, Comstock A H, McConnell A, Li X, Yun Y, Sun D and Xu X 2023 Giant interfacial spin Hall angle from Rashba-Edelstein effect revealed by the spin Hall Hanle process *Phys. Rev.* B **108** L241403

[116] Vogel A, Ruiz Caridad A, Nordlander J, Sarott M F, Meier Q N, Erni R, Spaldin N A, Trassin M and Rossell M D 2023 Origin of the critical thickness in improper ferroelectric thin films *ACS Appl. Mater. Interfaces* **15** 18482–92

[117] Akbashev A, Roddatis V, Vasiliev A, Lopatin S, Amelichev V A and Kaul A R 2012 Reconstruction of the polar interface between hexagonal $LuFeO_3$ and intergrown Fe_3O_4 nanolayers *Sci. Rep.* **2** 672

[118] Lee D, Yoon A, Jang S Y, Yoon J-G, Chung J-S, Kim M, Scott J F and Noh T W 2011 Giant flexoelectric effect in ferroelectric epitaxial thin films *Phys. Rev. Lett.* **107** 057602

[119] Zubko P, Catalan G and Tagantsev A K 2013 Flexoelectric effect in solids *Annu. Rev. Mater. Res.* **43** 387–421

[120] Li X *et al* Improper flexoelectricity in hexagonal rare-earth ferrites (arXiv:2409.17022)

[121] Griffin S M, Lilienblum M, Delaney K T, Kumagai Y, Fiebig M and Spaldin N A 2012 Scaling behavior and beyond equilibrium in the hexagonal manganites *Phys. Rev.* X **2** 041022

[122] Lin S-Z *et al* 2014 Topological defects as relics of emergent continuous symmetry and Higgs condensation of disorder in ferroelectrics *Nat. Phys.* **10** 970–7

[123] Wang X, Mostovoy M, Han M, Horibe Y, Aoki T, Zhu Y and Cheong S-W 2014 Unfolding of vortices into topological stripes in a multiferroic material *Phys. Rev. Lett.* **112** 247601

[124] Cheng S, Zhang D, Deng S, Li X, Li J, Tan G, Zhu Y and Zhu J 2018 Domain configurations in dislocations embedded hexagonal manganite systems: from the view of graph theory *Appl. Phys. Lett.* **112** 162905

[125] Chae S C, Horibe Y, Jeong D Y, Rodan S, Lee N and Cheong S-W 2010 Self-organization, condensation, and annihilation of topological vortices and antivortices in a multiferroic *Proc. Natl Acad. Sci.* **107** 21366

[126] Park H J, Tay R Y, Wang X, Zhao W, Kim J H, Ruoff R S, Ding F, Teo E H T and Lee Z 2019 Double-spiral hexagonal boron nitride and shear strained coalescence boundary *Nano Lett.* **19** 4229–36
[127] Zhao Y, Zhang C, Kohler D D, Scheeler J M, Wright J C, Voyles P M and Jin S 2020 Supertwisted spirals of layered materials enabled by growth on non-Euclidean surfaces *Science* **370** 6515442–445
[128] Wang Z-J *et al* 2024 Conversion of chirality to twisting via sequential one-dimensional and two-dimensional growth of graphene spirals *Nat. Mater.* **23** 331–8
[129] Han L *et al* 2022 High-density switchable skyrmion-like polar nanodomains integrated on silicon *Nature* **603** 63–67
[130] Sánchez-Santolino G *et al* 2024 A 2D ferroelectric vortex pattern in twisted $BaTiO_3$ freestanding layers *Nature* **626** 529–34
[131] Streubel R, Fischer P, Kronast F, Kravchuk V P, Sheka D D, Gaididei Y, Schmidt O G and Makarov D 2016 Magnetism in curved geometries *J. Phys. D: Appl. Phys.* **49** 363001
[132] Lu D, Baek D, Hong S, Kourkoutis L F, Hikita Y and Hwang H 2016 Synthesis of freestanding single-crystal perovskite films and heterostructures by etching of sacrificial water-soluble layers *Nat. Mater.* **15** 1255–60
[133] Zhang J *et al* 2024 Super-tetragonal $Sr_4Al_2O_7$ as a sacrificial layer for high-integrity freestanding oxide membranes *Science* **383** 388–94
[134] Ji D *et al* 2019 Freestanding crystalline oxide perovskites down to the monolayer limit *Nature* **570** 87–90
[135] Xu R *et al* 2020 Strain-induced room-temperature ferroelectricity in $SrTiO_3$ membranes *Nat. Commun.* **11** 3141
[136] Sun H *et al* 2023 Prominent size effects without a depolarization field observed in ultrathin ferroelectric oxide membranes *Phys. Rev. Lett.* **130** 126801
[137] Thomas R, Scott J F, Bose D N and Katiyar R S 2010 Multiferroic thin-film integration onto semiconductor devices *J. Phys.: Condens. Matter* **22** 423201
[138] Mikolajick T, Schroeder U and Slesazeck S 2020 The past, the present, and the future of ferroelectric memories *IEEE Trans. Electron Devices* **67** 1434–43
[139] Kim I-J and Lee J-S 2023 Ferroelectric transistors for memory and neuromorphic device applications *Adv. Mater.* **35** 2206864
[140] Meier D and Selbach S M 2022 Ferroelectric domain walls for nanotechnology *Nat. Rev. Mater.* **7** 157–73
[141] Han H *et al* 2018 Enhanced switchable ferroelectric photovoltaic effects in hexagonal ferrite thin films via strain engineering *ACS Appl. Mater. Interfaces* **10** 1846–53